



The Modern-Era Retrospective Analysis for Research and Applications, Version 2 (MERRA-2)

RONALD GELARO,^a WILL McCARTY,^a MAX J. SUÁREZ,^{a,b} RICARDO TODLING,^a ANDREA MOLOD,^a LAWRENCE TAKACS,^{a,c} CYNTHIA A. RANDLES,^{a,d,g} ANTON DARMENOV,^a MICHAEL G. BOSILOVICH,^a ROLF REICHLE,^a KRZYSZTOF WARGAN,^{a,c} LAWRENCE COY,^{a,c} RICHARD CULLATHER,^{a,e} CLARA DRAPER,^{a,b} SANTHA AKELLA,^{a,c} VIRGINIE BUCHARD,^{a,b} AUSTIN CONATY,^{a,c} ARLINDO M. DA SILVA,^a WEI GU,^{a,c} GI-KONG KIM,^a RANDAL KOSTER,^a ROBERT LUCCHESI,^{a,c} DAGMAR MERKOVA,^{a,c,h} JON ERIC NIELSEN,^{a,c} GARY PARTYKA,^{a,c} STEVEN PAWSON,^a WILLIAM PUTMAN,^a MICHELE RIENECKER,^a SIEGFRIED D. SCHUBERT,^{a,c} META SIENKIEWICZ,^{a,c} AND BIN ZHAO^{a,f}

^a Global Modeling and Assimilation Office, NASA Goddard Space Flight Center, Greenbelt, Maryland

^b Universities Space Research Association, Columbia, Maryland

^c Science Systems and Applications, Inc., Lanham, Maryland

^d Morgan State University, Baltimore, Maryland

^e Earth System Science Interdisciplinary Center, University of Maryland, College Park,

College Park, Maryland

^f Science Applications International Corporation, Beltsville, Maryland

(Manuscript received 20 October 2016, in final form 27 March 2017)

ABSTRACT

The Modern-Era Retrospective Analysis for Research and Applications, version 2 (MERRA-2), is the latest atmospheric reanalysis of the modern satellite era produced by NASA's Global Modeling and Assimilation Office (GMAO). MERRA-2 assimilates observation types not available to its predecessor, MERRA, and includes updates to the Goddard Earth Observing System (GEOS) model and analysis scheme so as to provide a viable ongoing climate analysis beyond MERRA's terminus. While addressing known limitations of MERRA, MERRA-2 is also intended to be a development milestone for a future integrated Earth system analysis (IESA) currently under development at GMAO. This paper provides an overview of the MERRA-2 system and various performance metrics. Among the advances in MERRA-2 relevant to IESA are the assimilation of aerosol observations, several improvements to the representation of the stratosphere including ozone, and improved representations of cryospheric processes. Other improvements in the quality of MERRA-2 compared with MERRA include the reduction of some spurious trends and jumps related to changes in the observing system and reduced biases and imbalances in aspects of the water cycle. Remaining deficiencies are also identified. Production of MERRA-2 began in June 2014 in four processing streams and converged to a single near-real-time stream in mid-2015. MERRA-2 products are accessible online through the NASA Goddard Earth Sciences Data Information Services Center (GES DISC).

1. Introduction

Reanalysis is the process whereby an unchanging data assimilation system is used to provide a consistent reprocessing of meteorological observations, typically

spanning an extended segment of the historical data record. The process relies on an underlying forecast model to combine disparate observations in a physically consistent manner, enabling production of gridded datasets for a broad range of variables, including ones that are sparsely or not directly observed. As such, and with appropriate consideration of the inherent uncertainties, reanalysis products have not only become a staple of the atmospheric research community, but are used increasingly for climate monitoring as well as for business applications in, for example, energy and

^g Current affiliation: ExxonMobil Research and Engineering Company, Annandale, New Jersey.

^h Current affiliation: I.M. System Group, Inc., Rockville, Maryland.

Corresponding author: Ronald Gelaro, ron.gelaro@nasa.gov

agriculture. Recent reanalyses from the National Oceanic and Atmospheric Administration (NOAA)/National Centers for Environmental Prediction (NCEP), the European Centre for Medium-Range Weather Forecasts (ECMWF), the National Aeronautics and Space Administration (NASA) Global Modeling and Assimilation Office (GMAO), and the Japan Meteorological Agency (JMA) provide a rich ensemble of climate data products beginning more or less with the period of regular conventional and satellite observations in the mid to late twentieth century (Saha et al. 2010; Dee et al. 2011; Rienecker et al. 2011; Kobayashi et al. 2015). However, there have also been successful efforts to extend atmospheric reanalyses back to the late nineteenth and early twentieth centuries using only surface pressure observations (Compo et al. 2011) or surface and mean sea level pressure observations plus surface marine winds (Poli et al. 2013). As noted by Dee et al. (2011), these century-long reanalyses have also sparked remarkable data recovery and digitization efforts by various groups around the world.

The GMAO's reanalysis development effort began (under its predecessor organization, the Data Assimilation Office) with the production of the Goddard Earth Observing System, version 1 (GEOS-1), reanalysis (Schubert et al. 1993) but advanced significantly with the more recent production of the Modern-Era Retrospective Analysis for Research and Applications (MERRA; Rienecker et al. 2011). MERRA encompassed the period 1979–2016 and was undertaken with two primary objectives: to place NASA's Earth Observing System (EOS) satellite observations in a climate context and to improve the representation of the atmospheric branch of the hydrological cycle compared with previous reanalyses. MERRA succeeded in meeting these objectives overall and was found to be of comparable quality to contemporaneous reanalyses produced by NCEP and ECMWF (e.g., Decker et al. 2011). However, it also suffered from a number of known, but not necessarily unique, deficiencies. These include unphysical jumps and trends in precipitation in response to changes in the observing system, biases and imbalances in certain atmospheric and land surface hydrological quantities, and a poor representation of the upper stratosphere (e.g., Bosilovich et al. 2011; Robertson et al. 2011; Reichle et al. 2011; Rienecker et al. 2011). In addition, the long-term viability of MERRA was limited by system constraints that precluded the incorporation of new satellite data sources beyond NOAA-18, which launched in 2005. At the time of its termination in March 2016, MERRA was at risk of suffering a significant degradation in quality were certain observing platforms to fail, including, for example, EOS *Aqua*, which was already well beyond its designed lifetime and provided MERRA with its only sources of hyperspectral infrared and afternoon-orbit microwave radiances.

The Modern-Era Retrospective Analysis for Research and Applications, version 2 (MERRA-2), was undertaken to provide a timely replacement for MERRA and to sustain GMAO's commitment to having an ongoing near-real-time climate analysis. MERRA-2 is intended as an intermediate reanalysis, one that leverages recent developments at GMAO in modeling and data assimilation to address some of the known limitations of MERRA but also provides a stepping stone to GMAO's longer-term goal of developing an integrated Earth system analysis (IESA) capability that couples assimilation systems for the atmosphere, ocean, land, and chemistry. Toward the latter goal, MERRA-2 includes aerosol data assimilation, thereby providing a multidecadal reanalysis in which aerosol and meteorological observations are jointly assimilated within a global data assimilation system. Other new developments in MERRA-2 relevant to IESA focus on aspects of the cryosphere and stratosphere, including the representation of ozone, and on the use of precipitation observations to force the land surface. At the same time, basic aspects of the MERRA-2 system, such as the variational analysis algorithm and observation handling, are largely unchanged since MERRA. Also unchanged is the preparation of most conventional data sources used originally in MERRA.

This paper presents an overview of MERRA-2, including a description of the data assimilation system and various measures of performance. Some of these measures focus on difficulties encountered in MERRA, while others highlight new capabilities, such as the assimilation of aerosol observations. This paper also serves as an introduction to a series of companion papers that provide more detailed analyses of the topics covered in this overview as well as others. For example, a detailed description of the MERRA-2 aerosol analysis system and its validation are presented in Randles et al. (2017) and Buchard et al. (2017, manuscript submitted to *J. Climate*, hereinafter B17). Reichle et al. (2017a,b) assess the land surface precipitation and land surface hydrology, while Draper et al. (2017, manuscript submitted to *J. Climate*) examine the land surface energy budget. Bosilovich et al. (2017) evaluate the global water balance and water cycle variability in MERRA-2. Collow et al. (2016) examine MERRA-2's representation of U.S. summer-time extreme precipitation events, and Lim et al. (2017) investigate aspects of major El Niño events. Collow and Miller (2016) examine the radiation budget and cloud radiative effect over the Amazon. Several papers investigate aspects of the stratosphere in MERRA-2: Wargan et al. (2017) examine the representation of lower-stratospheric ozone and the effect of assimilating

ozone observations from NASA's *Aura* satellite; [Coy et al. \(2016\)](#) examine the representation of the quasi-biennial oscillation in MERRA-2; and [Wargan and Coy \(2016\)](#) present a case study of the 2009 sudden stratospheric warming.

[Section 2](#) provides an overview of the MERRA-2 data assimilation system, focusing primarily on developments since MERRA, including new observation sources. Basic metrics of the assimilation system performance are presented in [section 3](#). The MERRA-2 aerosol analysis is described in [section 4](#), along with sample results and validation statistics. [Section 5](#) examines global and regional aspects of the representation of precipitation in MERRA-2, focusing on areas of difficulty in MERRA. Stratospheric processes and the representation of ozone are discussed in [section 6](#). [Section 7](#) addresses the representation of the cryosphere in MERRA-2, with focus on glaciated land surface processes. [Section 8](#) provides information about MERRA-2 products and how they can be accessed. It is noted here that each MERRA-2 data collection has its own digital object identifier (DOI) number, so data used in scientific publications can be cited exactly. Most of the results shown for MERRA-2 in this paper are derived from these collections, which are individually cited in the corresponding figure captions. Finally, a brief summary and perspective on future work are presented in [section 9](#). A list of acronyms is given in the [appendix](#).

2. MERRA-2 system description

MERRA-2 is produced with version 5.12.4 of the GEOS atmospheric data assimilation system. The key components of the system are the GEOS atmospheric model ([Rienecker et al. 2008](#); [Molod et al. 2015](#)) and the GSI analysis scheme ([Wu et al. 2002](#); [Kleist et al. 2009b](#)). The model includes the finite-volume dynamical core of [Putman and Lin \(2007\)](#), which uses a cubed-sphere horizontal discretization at an approximate resolution of $0.5^\circ \times 0.625^\circ$ and 72 hybrid-eta levels from the surface to 0.01 hPa. The analysis is computed on a latitude-longitude grid at the same spatial resolution as the atmospheric model using a 3DVAR algorithm based on the GSI with a 6-h update cycle and the so-called FGAT procedure for computing temporally accurate observation-minus-background departures. The analysis is applied as a correction to the background state using an IAU procedure ([Bloom et al. 1996](#)).

The MERRA-2 system has many of the same basic features as the MERRA system described in [Rienecker et al. \(2011\)](#) but includes a number of important updates. An overview of these updates is provided here, with additional details provided in companion publications as

cited. Unless otherwise stated, other aspects of the system configuration and preparation of the input data are as described in [Rienecker et al. \(2011\)](#). The updates discussed here include changes to the forecast model ([section 2a](#)), the analysis algorithm ([section 2b](#)), the observing system ([section 2c](#)), the radiance assimilation ([section 2d](#)), the bias correction of aircraft observations ([section 2e](#)), the mass conservation and water balance ([section 2f](#)), the precipitation used to force the land surface and drive wet aerosol deposition ([section 2g](#)), the boundary conditions for sea surface temperature and sea ice concentration ([section 2h](#)), and reanalysis production ([section 2i](#)).

a. Forecast model

Since MERRA, the GEOS model has undergone changes to both its dynamical core and its physical parameterizations. Whereas in MERRA the horizontal discretization of the model was computed on a latitude-longitude grid, MERRA-2 uses a cubed-sphere grid. This allows relatively uniform grid spacing at all latitudes and mitigates the more severe grid spacing singularities that occur on a latitude-longitude grid. Upgrades to the physical parameterization schemes include increased reevaporation of frozen precipitation and cloud condensate, changes to the background gravity wave drag, and an improved relationship between the ocean surface roughness and ocean surface stress ([Molod et al. 2015](#)). The MERRA-2 model also includes a Tokioka-type trigger on deep convection as part of the RAS convective parameterization scheme ([Moorthi and Suárez 1992](#)), which governs the lower limit on the allowable entrainment plumes ([Bacmeister and Stephens 2011](#)). A new glaciated land representation and seasonally varying sea ice albedo have been implemented, leading to improved air temperatures and reduced biases in the net energy flux over these surfaces ([Cullather et al. 2014](#)).

b. Analysis algorithm

The control variable for moisture used in recent versions of GSI and MERRA-2 differs from the one used in MERRA. Whereas MERRA used the so-called pseudorelative humidity ([Dee and da Silva 2003](#)) defined by the water vapor mixing ratio scaled by its saturation value, MERRA-2 uses the normalized pseudorelative humidity ([Holm 2003](#)) defined by the pseudorelative humidity scaled by its background error standard deviation. The latter has a near Gaussian error distribution, making it more suitable for the minimization procedure employed in the assimilation scheme. Also within the GSI, a tangent linear normal mode constraint ([Kleist et al. 2009a](#)) is applied during the minimization procedure to control noise and improve the overall use of observations. The background error statistics used in the

GSI have been updated as well in MERRA-2. As in MERRA, the statistics are estimated using the NMC method (Parrish and Derber 1992) by calculating variances and covariances from the differences between 24- and 48-h forecasts, but from a more recent version of GEOS. Compared with the MERRA system, the background error statistics for the MERRA-2 system exhibit generally smaller standard deviations for most variables, but both larger and smaller correlation length scales depending on the variable, latitude, and vertical level.

c. Observing system

MERRA included no new satellite observation sources after the introduction of *NOAA-18* in 2005. MERRA-2, in contrast, includes numerous additional satellite observations both before and after this time. The complete set of input observations assimilated in MERRA-2 is summarized in Table 1, while a detailed description of their use is provided in McCarty et al. (2016). Additions to the MERRA-2 observing system compared with MERRA include the following:

- atmospheric motion vectors from AVHRR;
- surface wind speeds from SSMIS;
- surface wind vectors from the *Meteorological Operational Satellite-A (MetOp-A)* ASCAT and WindSat;
- temperature and ozone profiles from EOS *Aura* MLS;
- total column ozone from EOS *Aura* OMI;
- bending angle from GPSRO;
- microwave and infrared sounding radiances from ATOVS on *NOAA-19*, *MetOp-A*, and *MetOp-B*;
- microwave sounding radiances from ATMS on *SNPP*;
- hyperspectral infrared radiances from IASI on *MetOp-A* and *MetOp-B* and from CrIS on *SNPP*; and
- geostationary radiances from MSG SEVIRI and Geostationary Operational Environmental Satellites (*GOES-11*, *GOES-13*, and *GOES-15*).

Time series of the various types of observations assimilated in MERRA and MERRA-2 are shown in Fig. 1. The number of assimilated observations in MERRA-2 grows from approximately 2 million per 6-h cycle in 2002 to almost 5 million in 2015, while MERRA assimilates approximately 1.5 million observations per 6-h cycle from 2002 onward. The GSI in MERRA-2 is also capable of assimilating microwave and hyperspectral infrared radiances from planned future satellites, including *MetOp-C* and *JPSS*. The temporary spike in the number of QuikSCAT data assimilated in MERRA-2 in late 2000 is due to an error in preprocessing, which led to observations beyond the midswath “sweet spot” being used in the analysis. This has no discernible impact on the quality

of the analyzed fields or on the use of other observations in the assimilation system.

MERRA-2 also assimilates reprocessed versions of some of the same satellite observation types used in MERRA. In MERRA-2, Remote Sensing Systems version 7 (RSS v7) recalibrated radiances and retrieved surface wind speeds from SSM/I are used, whereas MERRA used RSS v6. The use of retrieved ozone from the SBUV also differs, with MERRA-2 assimilating version 8.6 on 21 layers from 1980 through 2004 before switching to OMI and MLS in October 2004. In contrast, MERRA used SBUV version 8 throughout, in a form degraded from its original 21 layers to 12.

d. Radiance assimilation

Radiative transfer calculations necessary for the assimilation of satellite radiances in MERRA-2 are performed using the CRTM (Han et al. 2006; Chen et al. 2008). MERRA-2 uses version 2.1.3 of the CRTM for assimilation of all satellite radiances, whereas MERRA used a prototype version of the CRTM for all radiances except those from SSU, for which the GLATOVS (Susskind et al. 1983) was used. Differences between the prototype and version 2.1.3 of the CRTM are too numerous to mention here, but a detailed description of the latter can be found in Liu and Boukabara (2014).

The actively assimilated channels for each satellite sensor type in MERRA-2 are summarized in Table 2. Microwave temperature sounding channels with strong surface sensitivity—so-called window channels—are not assimilated in MERRA-2, in part because of the strong sensitivity of global precipitation and humidity to these data found in MERRA (Robertson et al. 2011). These include channels 1–3 and 15 on AMSU-A, channels 1–4 and 16 on ATMS, and channel 1 on MSU. For microwave humidity sounders including AMSU-B and MHS, window channels are actively assimilated along with the sounding channels. For heritage infrared sounders, channels 13–15 on HIRS were assimilated in MERRA but are excluded in MERRA-2. The channel selections for hyperspectral infrared sounders and performance assessments for selected instruments are provided in McCarty et al. (2016).

Like MERRA, MERRA-2 uses an automated bias correction scheme for the assimilation of most satellite radiance observations. Bias estimates for individual sensor channels are represented by a small number of predictors, which can depend on the atmospheric state, the radiative transfer model, and the sensor characteristics. Airmass- and viewing-angle-dependent biases are estimated using a variational scheme in which the

TABLE 1. Observation types assimilated in MERRA-2, including their usage dates and sources. Boldface fonts indicate observation types not assimilated in MERRA. Acronyms are defined in the appendix.

Data type	MERRA-2 dates	Source
Raob, pibal, and dropsonde	Conventional	
AIREP, PIREP, ASDAR, and MDCRS aircraft	1 Jan 1980–present 1 Jan 1980–present	See Rienecker et al. (2011) NCEP, ECMWF, and JMA
PAOB	1 Jan 1980–17 Aug 2010	BoM
Surface land	1 Jan 1980–present	NCEP
Surface ship and buoy	1 Jan 1980–present	ICOADS
Wind profiler	Ground-based remotely sensed	
NEXRAD VAD wind	14 May 1992–present 16 Jun 1997–present	UCAR and NCEP NCEP
GMS, MTSAT, and Himawari atmospheric motion vector	Satellite-derived wind	NCEP and JMA
Meteosat atmospheric motion vector	1 Jan 1980–present	NCEP and EUMETSAT
GOES atmospheric motion vector	1 Jan 1980–present	NCEP
AVHRR atmospheric motion vector	1 Oct 1982–present	CIMSS
SSM/I surface wind speed	9 Jul 1987–4 Nov 2009	RSS
<i>ERS-1</i> surface wind vector	5 Aug 1991–21 May 1996	ESA
<i>ERS-2</i> surface wind vector	19 Mar 1996–29 Mar 2011	ESA
QuikSCAT surface wind vector	19 Jul 1999–22 Nov 2009	JPL
MODIS atmospheric motion vector	2 Jul 2002–present	CIMSS and NCEP
SSMIS surface wind speed	23 Oct 2003–29 Oct 2013	RSS
WindSat surface wind vector	13 Aug 2007–4 Aug 2012	NCEP
ASCAT surface wind vector	15 Sep 2008–present	NCEP
SBUV and SBUV/2 ozone	Satellite retrieved	
SSM/I rain rate	1 Jan 1980–31 Sep 2004	NASA GES DISC
TMI rain rate	9 Jul 1987–16 Sep 2009	NASA GES DISC
MLS temperature	1 Jan 1998–8 Apr 2015	NASA GES DISC
MLS ozone	13 Aug 2004–present	NASA GES DISC
OMI total column ozone	1 Oct 2004–present	NASA GES DISC
GPSRO bending angle	1 Oct 2004–present	NASA GES DISC
TOVS	Radio occultation	
SSM/I	14 July 2004–present	NCAR and NCEP
ATOVS (<i>NOAA-15, NOAA-16, NOAA-17,</i> <i>and NOAA-18</i>)	Satellite radiance	
GOES sounder (<i>GOES-8, GOES-10, GOES-11,</i> <i>and GOES-12 low resolution</i>)	1 Jan 1980–10 Oct 2006	NCAR and NESDIS
AMSU-A (<i>Aqua</i>)	9 Jul 1987–4 Nov 2009	RSS
AIRS	21 Jul 1998–present	NESDIS
GOES sounder (<i>GOES-11, GOES-12, GOES-13,</i> <i>and GOES-15 full resolution</i>)	24 Apr 2001–31 Mar 2007	NCEP and NESDIS
ATOVS (<i>NOAA-19, MetOp-A, and MetOp-B</i>)	1 Sep 2002–present	NASA GES DISC
IASI	1 Sep 2002–present	NASA GES DISC
ATMS	1 Apr 2007–present	NESDIS
SEVIRI	21 May 2007–present	NESDIS
CrIS	17 Sep 2008–present	NESDIS
	16 Nov 2011–present	NESDIS
	15 Feb 2012–present	NESDIS
	7 Apr 2012–present	NESDIS

predictor coefficients are updated as part of the control vector used to minimize the analysis cost function ([Derber and Wu 1998](#)). Satellite scan-position-dependent bias is estimated directly as an exponential moving average filter of the observation-minus-background departures for brightness temperature. For both the variational and scan-position predictors, initial values of the coefficients

for MERRA-2 were derived from GEOS operations and other long production runs using system versions similar to that used for MERRA-2. In the few cases where no recent coefficient information was available, initial values were derived from MERRA. Note that no bias correction is applied to a small number of sensor channels that peak in the upper stratosphere, including

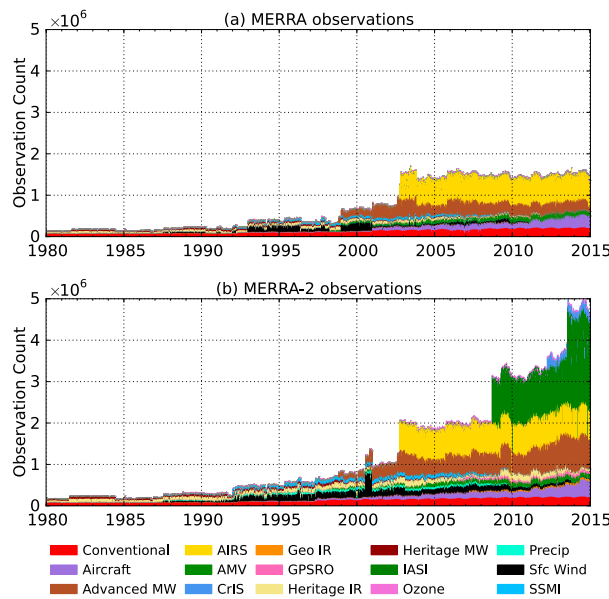


FIG. 1. Observations assimilated per 6-h cycle in (a) MERRA and (b) MERRA-2. The temporary spike in the number of surface wind observations assimilated in MERRA-2 in late 2000 is due to an error in the preprocessing of QuikSCAT data.

channel 14 on AMSU-A, channel 15 on ATMS, and channel 3 on SSU. This is done to prevent the variational bias correction scheme—which is formulated to remove systematic discrepancies between the observations and the background state irrespective of the source—from making erroneous adjustments to the observations at levels where model biases are known to be large.

e. Bias correction of aircraft temperature observations

A bias correction scheme for aircraft temperature observations has been implemented in MERRA-2, motivated by the known warm bias of these measurements compared with other data sources (Cardinali et al. 2003; Ballish and Kumar 2008; Rienecker et al. 2011). The scheme uses the mean observed-minus-background departures to estimate the bias for temperature reports from individual aircraft, identified by their tail number. The bias estimates are updated after each analysis. The scheme is used to correct AMDAR and ACARS reports only, since other sources of aircraft observations in MERRA-2 do not have unique identifiers by which they can be tracked. As of 2015, bias corrections for approximately 3700 separate aircraft are tracked in MERRA-2.

The performance of the scheme is discussed in McCarty et al. (2016). As expected, the scheme is shown to reduce the bias between the corrected aircraft observations and the background forecast, as well as to reduce the variance of the corrected background departures, allowing more

TABLE 2. Nominal channel selections for satellite radiances assimilated in MERRA-2. Usage can vary for individual satellite platforms as a result of sensor failure or quality control decisions.

Sensor	Assimilated channels
MSU	2–4
AMSU-A	4–14
ATMS	5–15 and 17–22
AMSU-B	1–5
MHS	1–5
SSM/I	1–7
SSU	1–3
HIRS	2–8 and 10–12
AIRS	See McCarty et al. (2016)
IASI	See McCarty et al. (2016)
CrIS	See McCarty et al. (2016)
GOES sounder	1–8 and 10–12
SEVIRI	2 and 3

aircraft observations to be used in the analysis. Unfortunately, the MERRA-2 background state was found to have a larger than expected positive bias in the mid to upper troposphere, which feeds back to the bias estimates. The result is that the bias correction actually increases the aircraft temperatures in some cases, and the fit to other unbiased observation types, such as radiosondes, is degraded. This is discussed further in section 3.

f. Mass conservation and water balance

Studies have documented the difficulty of maintaining realistic balances between variations in total mass and total water content in previous reanalyses (e.g., Trenberth and Smith 2005; Bosilovich et al. 2011; Berrisford et al. 2011). These studies show that analysis adjustments to moisture are often large (when, ideally, they should be small), highly sensitive to changes in the observing system, and mostly balanced by unphysical changes in precipitation. Takacs et al. (2016) argue that, in attempting to analyze the total mass of the atmosphere from surface pressure observations, reanalyses may violate the simple physical constraint that, to an excellent approximation, the total dry mass of the atmosphere is invariant, and so changes in total mass must be essentially equivalent to changes in total water mass. At the same time, Berrisford et al. (2011) argue that, while the observing system may not provide the data to determine exactly the total mass of the atmosphere, the degree to which dry mass is preserved in a reanalysis provides a useful diagnostic of reanalysis quality.

Reconsideration of these issues during the development of MERRA-2 prompted modifications to GEOS to conserve atmospheric dry mass and to guarantee that the net source of water from precipitation and surface evaporation equals the change in total atmospheric water. As described by Takacs et al. (2016), this has been

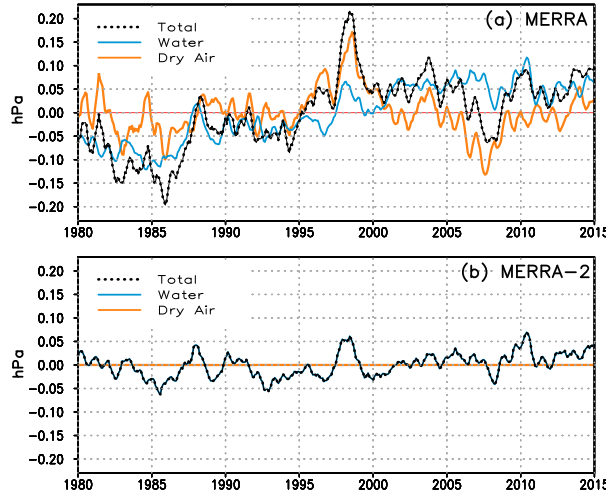


FIG. 2. Globally integrated monthly mean mass anomalies (hPa) from the mean seasonal cycle for (a) MERRA and (b) MERRA-2. Shown are the anomalies of total mass (black dotted), and their decomposition into atmospheric water (blue) and dry air (orange). Results for MERRA-2 are derived from the data collection described in GMAO (2015b).

achieved by making the following changes to the forecast model and assimilation procedure:

- Sources and sinks of atmospheric water have been added to the model continuity equation so that changes in total mass are driven purely by changes in total water.
- A constraint that penalizes analysis increments of dry air has been added to the GSI.
- Tendencies in the IAU are rescaled so that the global mean is removed from the analysis increment of water.

The global impact of these modifications is illustrated in Figs. 2 and 3, which compare different components of atmospheric mass in MERRA and MERRA-2. Figure 2 shows monthly mean anomalies from the mean seasonal cycle for total mass, total water, and dry-air mass in the two reanalyses. In MERRA, there is an increase in total water over the period, with significant interannual variations, but these features do not necessarily match the changes in total mass. There also are spurious anomalies in dry-air mass throughout, some of which track closely with the changes in total mass. In MERRA-2, changes in total mass and total water track each other almost perfectly, by design, and the dry-air mass remains a constant whose value must be specified. For the latter, the value 983.24 hPa is chosen based on MERRA. This value falls within 0.1% of the values derived from other recent reanalyses (Takacs et al. 2016).

Figure 3 shows monthly mean values of evaporation minus precipitation ($E - P$, or water source term), the vertically integrated analysis increment of water, and the

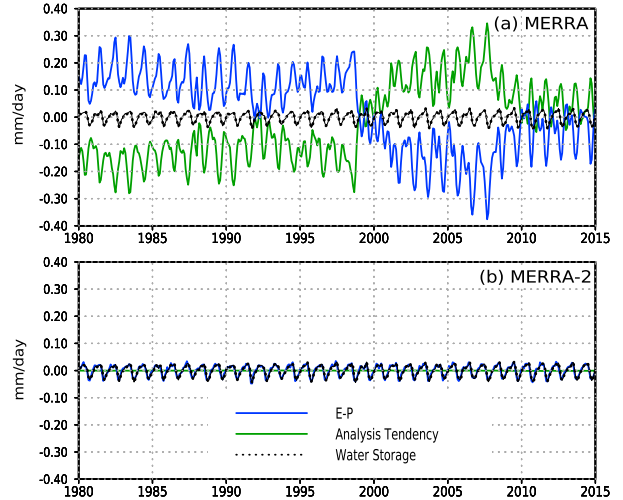


FIG. 3. Globally integrated monthly mean total water budget terms (mm day^{-1}) for (a) MERRA and (b) MERRA-2. Shown are the water source term ($E - P$; blue), vertically integrated analysis increment of water (green), and atmospheric water storage (black dotted). Results for MERRA-2 are derived from the data collections described in GMAO (2015b,d,e).

atmospheric water storage. Note that the atmospheric water storage has similar magnitude in both reanalyses and is dominated by the seasonal cycle. In MERRA, however, the storage is determined by a near balance between the large and highly variable contributions from the analysis increment on the one hand, and unphysical variations in $E - P$ of the opposite sign on the other hand. This includes an abrupt change in the sign of these quantities after the introduction of AMSU-A in 1998 (Robertson et al. 2011). In MERRA-2, the globally integrated analysis increment is zero, by design, and the water storage is determined as in nature by small seasonal differences in E and P . It should be noted that removing the global mean analysis increments of total mass and water mass does not imply that the analysis increments of water vapor or surface pressure vanish locally, as shown in section 3 of this paper and discussed in further detail by Bosilovich et al. (2017).

g. Observation-corrected precipitation forcing

The precipitation generated by the atmospheric model during the IAU segment of the assimilation procedure is subject to considerable errors that can propagate into land surface hydrological fields and beyond (Reichle et al. 2011). To mitigate these effects in MERRA-2, the model-generated precipitation is corrected with observations before being used to force the land surface or affect the wet deposition of aerosols over land and ocean. Both the model-generated precipitation and the precipitation seen by the land surface and the

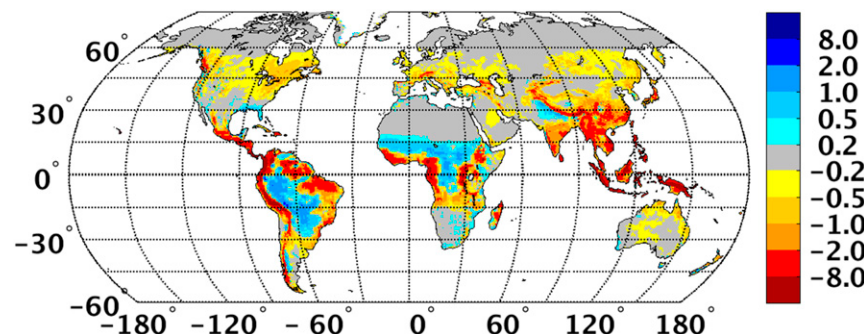


FIG. 4. Mean difference (1980–2015; mm day^{-1}) between the (corrected) MERRA-2 precipitation seen by the land surface and the model-generated precipitation within the MERRA-2 system. Results are derived from the data collections described in GMAO (2015h,j).

aerosols are available in the MERRA-2 output. MERRA-2 is one of several recent applications of GEOS that uses observation-corrected precipitation estimates. Others include the GMAO seasonal forecasting system (Ham et al. 2014), the MERRA-Land data product (Reichle et al. 2011), and the aerosol reanalysis MERRAero (Buchard et al. 2015). Precipitation observations have also been used in reanalyses produced by NOAA, including the North American Regional Reanalysis (Mesinger et al. 2006) and in the CFSR (Saha et al. 2010; Meng et al. 2012), although in both cases the approaches differ from that used in MERRA-2. Some discussion of the differences between the approaches used in MERRA-2 and CFSR can be found in Reichle et al. (2017a).

The corrected precipitation in MERRA-2 is derived from publicly available, observationally based global precipitation products disaggregated from daily or pentad totals to hourly accumulations using precipitation estimates from MERRA (Reichle and Liu 2014; Reichle et al. 2017a). The land surface in MERRA-2 sees a combination of corrected and model-generated precipitation depending on latitude, with the land surface forced primarily by the corrected estimates at low to midlatitudes, by the MERRA-2 model-generated precipitation at high latitudes, and by a weighted mixture in between to prevent spatial discontinuities in climatological means. This is illustrated in Fig. 4, which shows the annual average adjustment made to the model-generated precipitation in MERRA-2 for the period 1980–2015 using this technique. The greatest adjustments are made in the tropics, where precipitation is greatest and the corrected estimates are given most weight, while no adjustments are made poleward of 62.5° latitude in either hemisphere.

Based on the evaluation of several metrics, Reichle et al. (2017a) found the observation-corrected precipitation to be more realistic overall than that generated by the model within the cycling MERRA-2 system, or that of the

MERRA and MERRA-Land data products. Exceptions include discontinuities in the MERRA-2 corrected precipitation that result from errors in the underlying gauge products, for example, in Myanmar and South America. Another issue is the high bias in MERRA-2 summer precipitation in the high latitudes (where precipitation observations are not used). Moreover, the diurnal cycle of the MERRA-2 corrected precipitation has reasonable amplitudes compared to independent observations, but the time of day of maximum precipitation is inherited from MERRA and is unrealistic.

The improvements in the precipitation forcing are also reflected in the MERRA-2 land surface estimates. Reichle et al. (2017b) show that soil moisture, snow, terrestrial water storage, and runoff in MERRA-2 agree better with independent observations than estimates from MERRA. Draper et al. (2017, manuscript submitted to *J. Climate*) further demonstrate that the temporal behavior and long-term mean values of the land–atmosphere turbulent fluxes in MERRA-2 are improved. Moreover, by applying the precipitation corrections within the coupled atmosphere–land modeling system, MERRA-2 can provide more self-consistent surface meteorological data than were used for MERRA-Land (Reichle et al. 2017a). This self-consistency is important for applications such as forcing land-only model simulations.

Finally, it should be noted that the atmospheric water and energy prognostic variables associated with the creation of precipitation in MERRA-2 are not directly modified by the corrected estimates, although they can be indirectly modified through subsequent feedback with the land surface.

h. Sea surface temperature and sea ice concentration

The boundary conditions for SST and SIC in MERRA were based on the 1° resolution weekly (or monthly) product of Reynolds et al. (2002). In MERRA-2, SST and SIC boundary conditions are instead based on

TABLE 3. Sea surface temperature and sea ice concentration data products used in MERRA-2.

MERRA-2 dates	SST and SIC product
1 Jan 1980–31 Dec 1981	CMIP midmonthly 1°
1 Jan 1982–31 Dec 2002	NOAA OISST daily 1/4° (AVHRR)
1 Jan 2003–31 Mar 2006	NOAA OISST daily 1/4° (AVHRR and AMSR-E)
1 Apr 2006–present	OSTIA daily 1/20°

currently available high-resolution (finer than 1° resolution) daily products. However, as there exists no continuous source of daily global high-resolution SST and SIC for the entire period of MERRA-2—and no source of daily data whatsoever prior to 1982—the following products were used in combination (Table 3): monthly 1° resolution data from CMIP as in Taylor et al. (2000) for the period prior to 1982; daily 1/4° resolution data from NOAA OISST as in Reynolds et al. (2007) from 1982 through March 2006; and daily 1/20° resolution data from OSTIA as in Donlon et al. (2012) from April 2006 onward. Note that different versions of the NOAA OISST product are used prior to and after January 2003, the latter including satellite data from both AVHRR and AMSR-E on NASA's *Aqua* satellite, and the former including satellite data from AVHRR only. The processing of these products into a unified gridded set of daily SST and SIC boundary conditions for MERRA-2 is described in Bosilovich et al. (2015). Care was taken to use both SST and SIC from the same data source to avoid potential inconsistencies, especially in marginal ice zones.

Figure 5 shows 12-month running averaged values of SST between 60°N and 60°S for MERRA-2 and several other reanalyses, including MERRA. In all cases, there is a positive trend in SST throughout the period. The running means for all the reanalyses are within 1 K for the 30 years spanning 1980–2010, and the anomalies (not shown) are separated by less than 0.2 K. At the same time, there are clear systematic differences between reanalyses, with the MERRA-2 SST's on the one hand being cooler than those used in the other reanalyses shown except CFSR (which used similar input datasets), especially before the transition to OSTIA in 2006. The values for JRA-55, on the other hand, are on the order of 0.1 K higher than other reanalyses throughout the 35-yr period. It can also be seen that the MERRA-2 SSTs increase slightly with the change in NOAA OISST versions after 2003. The reader is referred to Bosilovich et al. (2015) for a more detailed list of known issues with the SST and SIC boundary conditions for MERRA-2.

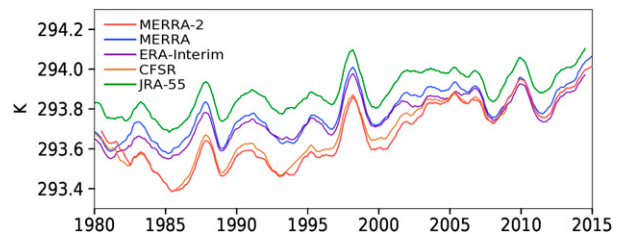


FIG. 5. Time series of 12-month running mean prescribed SST (K) for various reanalyses, averaged between 60°N and 60°S. Results for MERRA-2 are derived from the data collection described in GMAO (2015f).

i. Production

MERRA-2 was produced in four separate streams, each of which was spun up for a year at full resolution beginning on 1 January 1979 (stream 1), 1 January 1991 (stream 2), 1 January 2000 (stream 3), and 1 January 2010 (stream 4). The land surface restart files for each MERRA-2 stream were themselves spun up for at least 20 years using the offline MERRA-2 land model forced by MERRA surface meteorological fields, and with the precipitation replaced by the observation-corrected estimates described in section 2g. The final MERRA-2 product distribution is from stream 1 for 1 January 1980–31 December 1991, followed by stream 2 for 1 January 1992–31 December 2000, then stream 3 for 1 January 2001–31 December 2010, and finally stream 4 for 1 January 2011–present. With streams 1–3 complete, MERRA-2 production continues as a near-real-time climate analysis from stream 4 alone. The decision to begin stream 1 in January 1979 and distribute products beginning in January 1980—a year later than the schedule followed in MERRA—was based on the fact that the products used to create the observation-corrected precipitation estimates for MERRA-2 only start on 1 January 1979, leaving no viable way to initialize the land surface properly before this time (which requires several months of spinup after initialization from climatological conditions).

The overlap periods between successive streams were examined to determine the adequacy of the spinup procedure and to quantify the uncertainty in individual fields. Differences between overlapping MERRA-2 streams were found to be minimal for most fields after one year, with the exception of certain land surface variables including the deep-level soil temperature and land surface soil moisture storage at high latitudes. The spinup of the land surface is addressed separately in Reichle et al. (2017a); section 3d and Fig. 13 of that paper discuss specific examples of the aforementioned discontinuities across consecutive MERRA-2 streams. Users should be aware of these

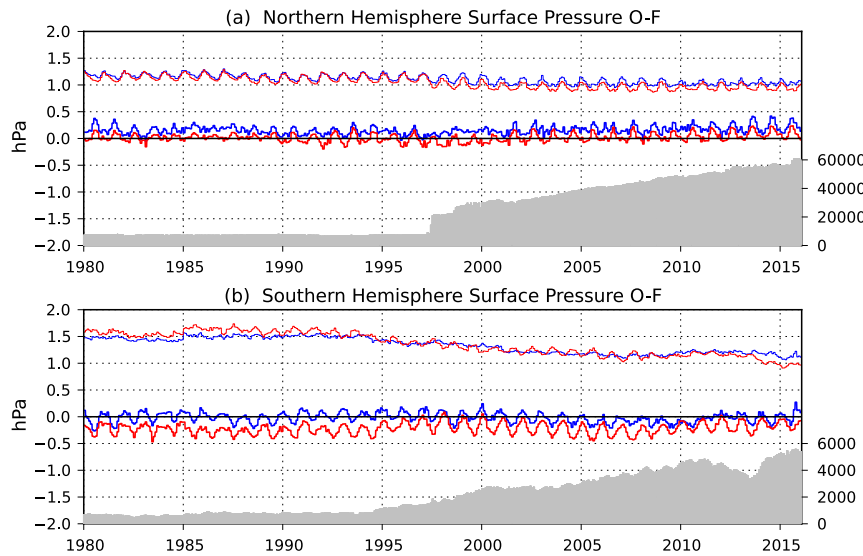


FIG. 6. Monthly mean (thick lines) and RMS (thin lines) background departures for surface pressure observations (hPa) assimilated in MERRA (blue) and MERRA-2 (red). Results are shown for the (a) Northern Hemisphere and (b) Southern Hemisphere. Also shown are the corresponding monthly mean counts of surface pressure observations assimilated in MERRA-2 (gray shaded).

discontinuities when the data are used for specific applications.

3. Data assimilation diagnostics

By-products of the data assimilation procedure in the form of differences between forecasts and observations, analysis increments, and estimates of bias can be used effectively to monitor the quality of both the input and output of the assimilation. In this section, examples of such diagnostics are presented for MERRA-2, focused mainly on feedbacks with respect to in situ conventional observations and on the net correction, or increment, brought by the entirety of the assimilated observations. The reader is referred to McCarty et al. (2016) for examples of feedbacks related to the treatment of satellite radiance observations.

a. Background departure statistics

Differences between the assimilated observations and the background forecast, referred to as innovations or background departures, provide important information about the quality of the assimilation. In particular, it is important that the assimilation system be able to predict high-quality observations, especially for conventional data types that provide direct measurements of the analyzed variables. In addition to affecting the analysis directly, many conventional data play an important role in anchoring the variational bias estimates used in the

assimilation of satellite radiances. Generally speaking, smaller background departures indicate a higher-quality assimilation. The results shown here are selected to highlight both strengths and weaknesses of MERRA-2 in this regard. As in MERRA, for convenience, gridded versions of the observations and corresponding departures used in MERRA-2 will be made available to users.

Figure 6 shows time series of monthly mean and RMS background departure statistics for all assimilated surface pressure observations in MERRA and MERRA-2 for both the Northern and Southern Hemisphere. Also shown are the monthly mean numbers of surface pressure observations assimilated in each 6-h assimilation cycle in MERRA-2. The RMS values decrease with time in both reanalyses, especially in the Southern Hemisphere after the early to mid-1990s, when the number of observations begins to increase significantly. The RMS values in the Northern Hemisphere (Fig. 6a) are smaller than in the Southern Hemisphere initially and decrease more slowly with time, reflecting the greater number of conventional observations available over land throughout the period. This decrease is slightly more pronounced in MERRA-2 after the mid-1990s when the number of surface pressure observations from land stations increases significantly. In the Southern Hemisphere (Fig. 6b), the RMS values are larger in MERRA-2 than in MERRA before the mid-1990s but smaller by the end of the period. The larger values early on are due to the use of larger observation errors for surface ship observations (and some other

conventional data types) in MERRA-2, allowing more “outliers” with larger departure values to pass the quality control procedure in the analysis.¹ The impact diminishes by the mid-1990s as other observation types, including from satellites, become more abundant. There is no similar effect in the Northern Hemisphere, where surface pressure observations from land stations are dominant early in the period; the observation errors specified for these data are the same in MERRA and MERRA-2. Finally, the jump in RMS values in the Southern Hemisphere evident in both reanalyses at the beginning of 1985 coincides with the introduction of regularly spaced synthetic surface pressure observations over Southern Ocean areas.

The mean background departures for surface pressure in the Northern Hemisphere are consistently less biased in MERRA-2 than in MERRA, especially after the mid-1990s. In the Southern Hemisphere, however, the departures for MERRA-2 show a negative bias throughout the period; this is discussed further in section 3b. The mean departures in MERRA-2 also show a more pronounced annual cycle in this hemisphere. As a point of reference, the background departure statistics for other reanalyses, including, for example, ERA-Interim (Dee et al. 2011), exhibit a clear annual cycle, but with somewhat smaller amplitude than in MERRA-2.

Figure 7 shows global background departure statistics for radiosonde temperatures for MERRA and MERRA-2 at selected pressure levels in the troposphere (300 and 700 hPa) and stratosphere (10 and 50 hPa). Also shown for each level are the monthly mean numbers of radiosonde temperature observations assimilated in each 6-h assimilation cycle in MERRA-2. In the troposphere (Figs. 7c,d), the performance of MERRA-2 is degraded compared to that of MERRA, especially at 300 hPa. The RMS values for MERRA-2 decrease with time but remain 10%–20% larger than those for MERRA during much of the period. Again, this is due at least partially to the use of larger observation errors for radiosonde temperatures and other conventional data types in MERRA-2. Noticeable improvements occur first in the mid-1990s, when satellite observations become more abundant, and again in 2006, when the number of GPSRO observations increases significantly.

The mean departure values at 300 hPa for both MERRA and MERRA-2 exhibit a clear negative bias. The bias is generally larger in MERRA-2, reaching a maximum amplitude of greater than 0.5 K during the early 2000s. This is due to a warm model bias in the

upper troposphere, which worsened during the course of development between MERRA and MERRA-2 (see also Fig. 10). However, aspects of the assimilation process may exacerbate the problem. It can be seen, for example, that the bias in the background departures at 300 hPa increases noticeably after the mid-1990s, especially in MERRA-2, when the numbers of both aircraft temperature observations and satellite radiances begin to increase significantly (Fig. 1). The design of the bias correction procedures for both observation types is such that they result in an adjustment of the observations regardless of the source of the bias. In the presence of a strong model bias this can reinforce the actual observational bias and cause the assimilation system to drift further toward the model state, as noted in the case of the aircraft bias corrections described in section 2e. A similar, though less direct, effect may occur through the observational bias corrections used to assimilate satellite radiances, although other aspects of the variational scheme used to adjust these data act to reduce this risk (Dee and Uppala 2009). At 700 hPa, the mean departures for both reanalyses are generally more comparable and considerably less biased.

In the stratosphere (Figs. 7a,b), there are fewer significant differences between the results for MERRA and MERRA-2, although the departures at 10 hPa for MERRA-2 show a larger negative bias from -0.2 to -0.3 K prior to the early 2000s. After 2002, when assimilation of AIRS radiances begins, the biases at 10 hPa in both reanalyses exhibit an upward trend and eventually become positive, first in MERRA around 2003 and then in MERRA-2 in 2005. There is a discernible jump in the mean departures at this level for MERRA-2 in 2005. This is around the time when assimilation of both MLS temperature retrievals (above 5 hPa) and GPSRO bending angle observations (up to approximately 10 hPa) begins in MERRA-2, but this does not appear to improve the fit to radiosondes at 10 hPa compared with MERRA. After 2006, the biases in both reanalyses have average values of 0.2 – 0.3 K. Finally, at 50 hPa, the departure values for both reanalyses are very similar and exhibit only a small positive bias throughout.

Figure 8 shows statistics for radiosonde specific humidity background departures at 500 and 850 hPa in the tropics. The performance of MERRA-2 is slightly worse than that of MERRA in the midtroposphere in terms of both RMS and bias, but similar or slightly better in the lower troposphere. Again, the mean departure values are consistent with known biases in the GEOS model.

b. Analysis increments

The analysis increments represent the net adjustment to the background state by the assimilation scheme in response to all the observations. As this

¹ The observation errors for conventional data types have been adjusted since MERRA-2.

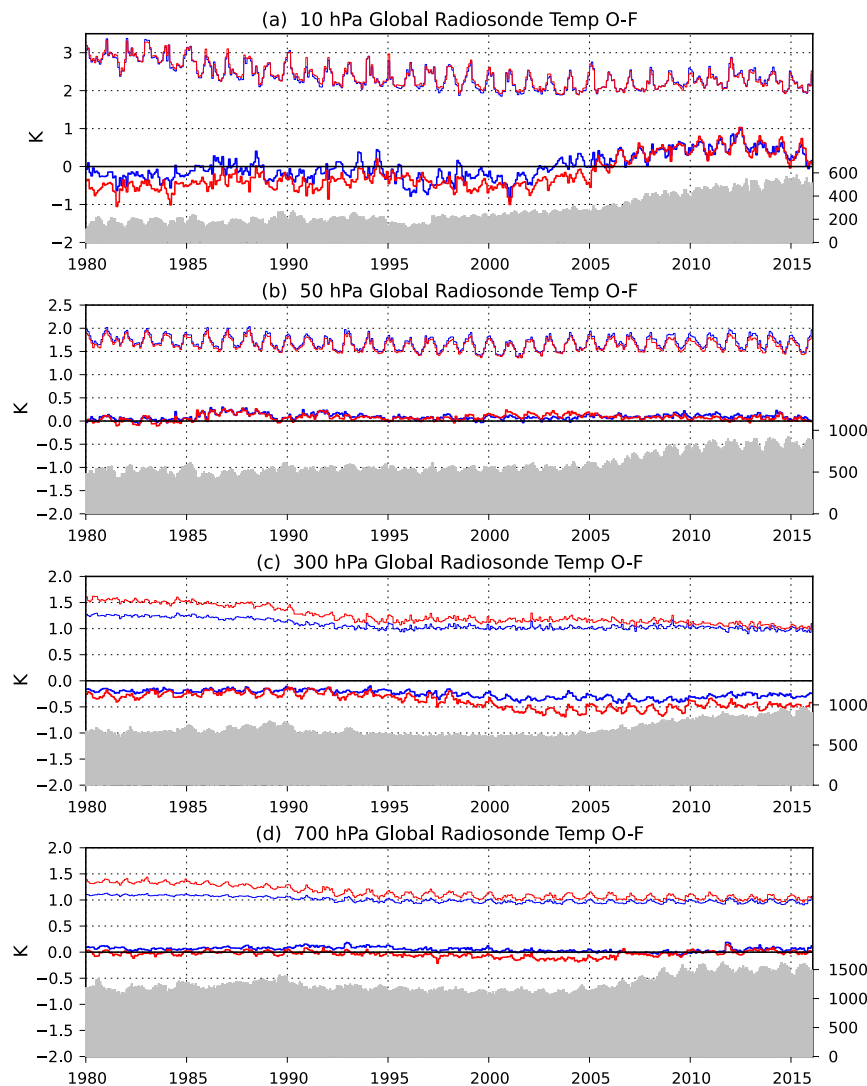


FIG. 7. Global monthly mean (thick lines) and RMS (thin lines) background departures for radiosonde temperature observations (K) assimilated in MERRA (blue) and MERRA-2 (red). Results are shown for the pressure levels (a) 10, (b) 50, (c) 300, and (d) 700 hPa. Also shown are the corresponding monthly mean counts of radiosonde temperature observations assimilated in MERRA-2 (gray shaded).

adjustment depends in a complex way on assumed or crudely estimated errors in the observations and background state, and on the forward operator that transforms the model variables to observation space, the increments do not necessarily represent errors in the background state. Nonetheless, their spatial and temporal variations provide an important diagnostic of system performance, including how changes in the observing system may affect the consistency of the analysis. Systematic increments often indicate the presence of biases in the model or observations that may complicate the use of reanalyses for estimating budgets and identifying trends (Dee et al. 2011).

As described in section 2, the GEOS assimilation system uses an IAU procedure, which, instead of correcting the initial condition, applies the analysis increment to the model as a constant tendency term during the 6-h assimilation window. It is this contribution to the time tendency from the analysis that is provided as a standard output quantity in MERRA-2, examples of which are presented here. For convenience, these are referred to as simply the analysis increments in the discussion that follows.

Figure 9 shows the mean and standard deviation in time of the monthly mean analysis increment of surface pressure in MERRA-2 for the period January 1980

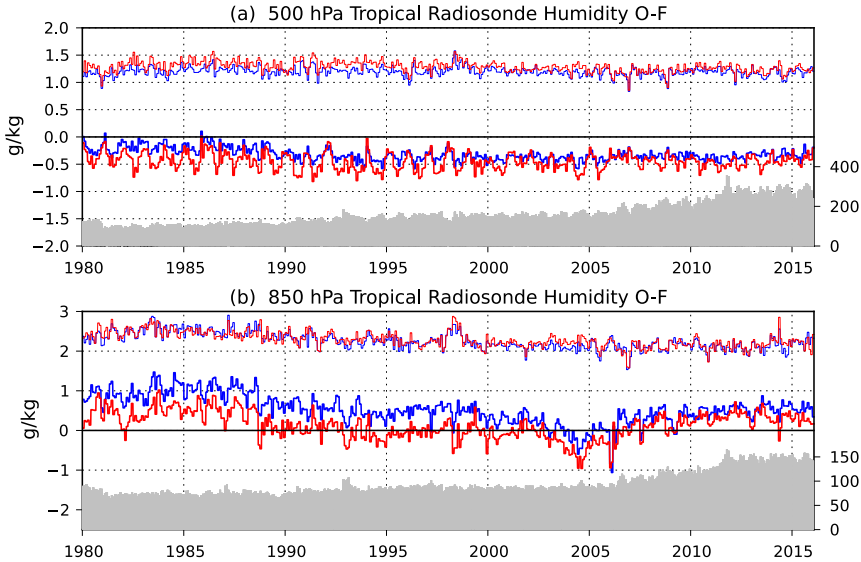


FIG. 8. As in Fig. 7, but for radiosonde specific humidity observations (g kg^{-1}) in the tropics (20°N – 20°S) at (a) 500 and (b) 850 hPa.

through December 2015. The monthly means themselves have been computed from subdaily data, eight times per day. The pattern of the mean increments indicates that the analysis tends to move mass from the oceans to the continents, as noted also by Takacs et al. (2016), although this pattern is arguably most robust in the Southern Hemisphere. (The mostly negative surface pressure increments over Canada provide an obvious counterexample.) These results are consistent with those in Fig. 6 showing a negative bias in the Southern Hemisphere background departures in MERRA-2. The standard deviation of the increments shows that the largest variations in surface pressure occur in the middle and high latitudes, and especially over coastal Antarctica and the mountainous regions of southern and eastern Asia, as well as southern Alaska.

Time series of the global monthly mean and standard deviation of the analysis increments of temperature from the surface to 70 hPa in MERRA-2 are shown in Fig. 10. The most striking feature in the mean increments is the persistent cooling by the analysis in the layer between 250 and 400 hPa. This is consistent with the negative bias in the background departures at 300 hPa shown in Fig. 7 and provides further evidence of the warm model bias at these levels. Except for seasonal variations, the magnitude of the cooling remains relatively constant throughout much of the period, although noticeable changes occur, for example, beginning in the mid-to-late 1990s as the number of aircraft and satellite observations increase, and again in 2006, possibly in response to the introduction of data from IASI and GPSRO. Warming by the analysis is evident above 200 hPa and

below 700 hPa. In this global view, the mean increments close to the surface exhibit a negative trend, with strong warming before the early 1990s turning to slight cooling after 2010, but this is in fact the net effect of distinct

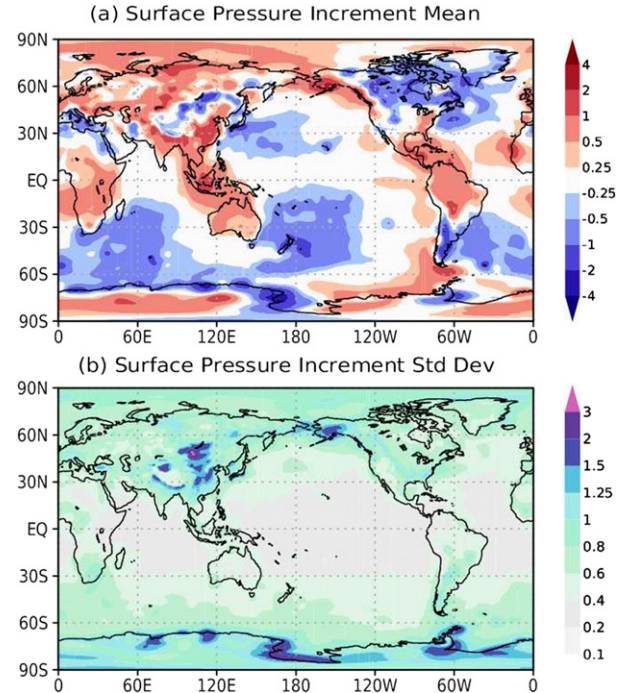


FIG. 9. (a) Mean and (b) standard deviation of the monthly mean analysis tendency of surface pressure (hPa day^{-1}) for the period January 1980 through December 2015. Monthly mean values are based on four synoptic times daily. Results are derived from the data collection described in GMAO (2015k).

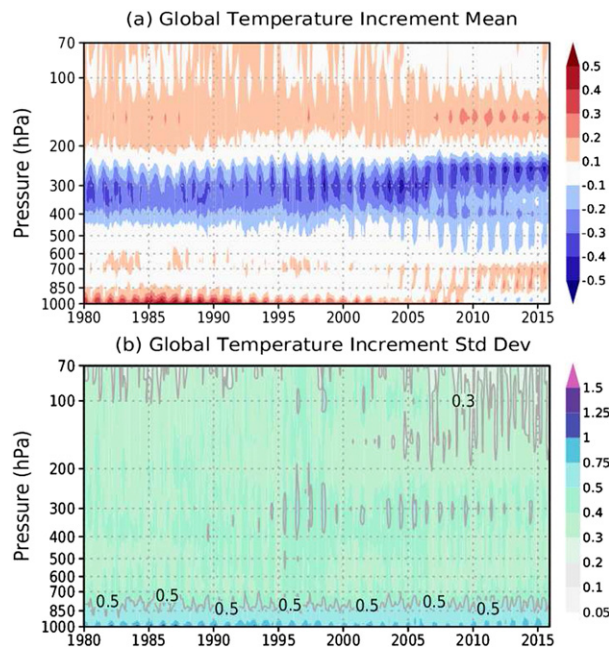


FIG. 10. Global (a) mean and (b) standard deviation of the monthly mean analysis tendency of temperature (K day^{-1}) from 1000 to 70 hPa. Monthly means values are based on four synoptic times daily. Results are derived from the data collection described in GMAO (2015n).

regional differences in the increments (not shown). In particular, near-surface warming by the analysis in response to a cold model bias over northern midlatitude landmasses is offset by cooling over southern oceans that generally increases with time, beginning with the assimilation of data from the first microwave humidity sensors in the late 1980s. These differences also contribute to the large variability of the increments below 700 hPa (Fig. 10b). The variability in the midtroposphere is noticeable but small compared with that at low levels, again highlighting the consistency of the cooling by the observations between 250 and 400 hPa.

The increments of specific humidity in the tropics are shown in Fig. 11 for levels between the surface and 250 hPa (the values become exceedingly small above this level). The mean increments indicate distinct biases in the middle and lower troposphere, with systematic drying between 600 and 300 hPa and mostly moistening below 700 hPa. The corrections are generally larger during the second half of the period and especially after the late 1990s as more satellite observations of humidity become available. There is an abrupt increase in the variability of the increments corresponding to the introduction of the first SSM/I instrument in mid-1987, with additional increases corresponding to the use of a second and third SSM/I instrument in late 1990 and mid-1995, respectively. The use of multiple SSM/I instruments from the early

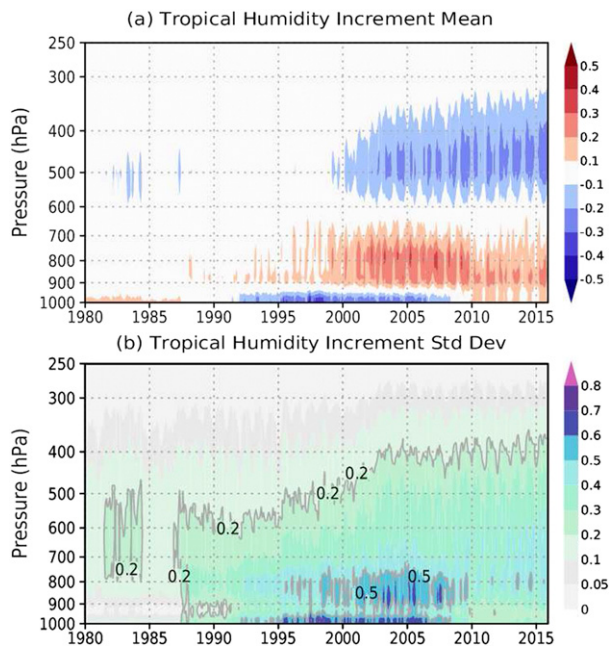


FIG. 11. As in Fig. 10, but for specific humidity ($\text{g kg}^{-1} \text{ day}^{-1}$) in the tropics (20°N – 20°S) from 1000 to 250 hPa. Results are derived from the data collection described in GMAO (2015).

1990s to late 2000s also corresponds to a strong drying and a marked increase in variability at levels very close to the surface. The introduction of AMSU-B data in 1998 corresponds to marked increases in the mean and variability of the increments, the latter being most pronounced in the layer between 800 and 900 hPa. The sensitivity of the precipitation to these observing system changes is discussed in section 5.

4. Aerosol data assimilation

In addition to a standard meteorological analysis, MERRA-2 includes an aerosol analysis as described in Randles et al. (2016, 2017) and B17. The multidecadal coverage and the coupling between aerosols and the circulation is a step forward compared to previous EOS-era reanalyses, such as MERRAero, the NAAPS reanalysis (Lynch et al. 2016), the MACC reanalysis (Inness et al. 2013), and the more recent CAMS reanalysis (Flemming et al. 2017). The MERRA-2 system produces 3-hourly analyses and gridded output of both observable parameters and aerosol diagnostics not easily observed, especially on a global scale, with potential applications ranging from air quality forecasting to studies of aerosol-climate and aerosol-weather interactions (e.g., Bocquet et al. 2015).

An analysis splitting technique (Randles et al. 2017) is used to assimilate AOD at 550 nm, in which a

two-dimensional analysis is performed first using error covariances derived from innovation data, and then the horizontal increments are projected vertically and across species using an ensemble method. AOD observations are derived from several sources, including

- reflectances from AVHRR [1979–2002, ocean-only ([Heidinger et al. 2002](#))],
- reflectances from MODIS on *Terra* (2000–present) and *Aqua* (2002–present) ([Remer et al. 2005; Levy et al. 2007](#)),
- AOD retrievals from MISR [2000–14, bright, desert regions only ([Kahn et al. 2005](#))], and
- direct AOD measurements from the ground-based AERONET [1999–2014 ([Holben et al. 1998](#))].

MODIS provides the vast majority of AOD observations assimilated in MERRA-2, especially after 2002, when data from both the *Terra* and *Aqua* satellites become available. Prior to 2000, only AVHRR reflectances over ocean are used in MERRA-2. AOD for both MODIS and AVHRR are derived from cloud-cleared reflectances using a neural net procedure trained on AERONET measurements ([Randles et al. 2017](#)). By construction, these AOD retrievals are unbiased with respect to AERONET observations. AOD from MISR and AERONET observations are used without bias correction. Additional details about the aerosol observing system in MERRA-2 can be found in [Randles et al. \(2016, 2017\)](#).

The GOCART model ([Chin et al. 2002; Colarco et al. 2010](#)) is coupled with the GEOS atmospheric model to simulate the life cycles of five externally mixed aerosol species, including dust, sea salt, black carbon, organic carbon, and sulfate. The model carries three-dimensional mass mixing ratios of these five aerosol species as prognostic aerosol tracers. The AOD at 550 nm is a column- and species-integrated optical quantity, which is calculated as the summed product of each species mass and its extinction coefficient based on aerosol optical properties derived largely from the OPAC dataset [see [Randles et al. \(2017\)](#) and references therein]. Emissions of both dust and sea salt are wind-driven for each of five size bins, parameterized following [Marticorena and Bergametti \(1995\)](#) and [Gong \(2003\)](#), respectively. Sulfate and carbonaceous aerosol emissions derive from both natural and anthropogenic sources, as described in [Randles et al. \(2017\)](#). In particular, MERRA-2 includes volcanic sources ([Diehl et al. 2012](#)) and biomass burning emissions that utilize satellite observations and are based on the Reanalysis of the Tropospheric Chemical Composition, version 2 (RETRO-2; [Schultz et al. 2008](#)), the Global Fire Emissions Database, version 3.1 (GFED-3.1; [van der Werf et al. 2006](#)), and the

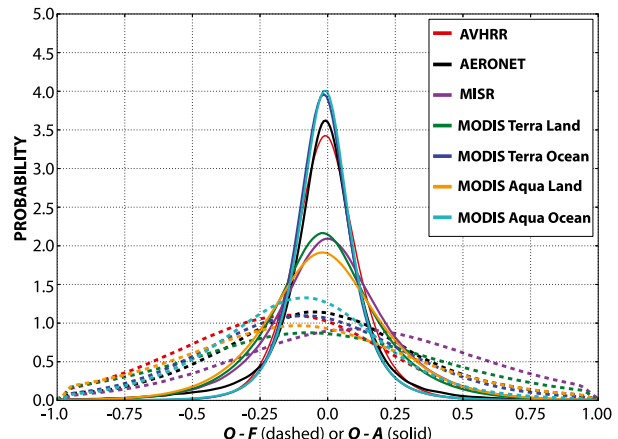


FIG. 12. Probability distribution functions (PDFs) of observation minus forecast ($O - F$; dashed) and observation minus analysis ($O - A$; solid) differences in observation space, collocated in space and time for each sensor in the MERRA-2 aerosol observing system. The PDFs are calculated from innovation data in log-transformed space [$\ln(\text{AOD} + 0.01)$] to ensure distributions are positive and Gaussian. The time periods considered include AVHRR (1993–99; red), MODIS *Terra* (2001–14; green and blue), MODIS *Aqua* (2003–14; orange and cyan), MISR (2001–12; purple), and AERONET (2000–13; black).

Quick Fire Emission Dataset, version 2.4r6 (QFED-2.4.r6; [Darmenov and da Silva 2015](#)).

It should be noted that AOD observations can only directly constrain the total, species-integrated and vertically integrated aerosol extinction—a quantity that can be related to column aerosol mass by assuming a set of optical properties. Nonanalyzed aerosol properties, such as the vertical distribution, aerosol speciation, and absorption, are not fully constrained by the observations and are chiefly determined by the underlying model physics and error covariance assumptions. Despite this fact, B17 show that the MERRA-2 aerosol reanalysis has considerable skill in simulating numerous observable aerosol properties. [Randles et al. \(2017\)](#) show that the AOD fields in MERRA-2 generally have both high correlation and low bias relative to independent (non-assimilated) sun photometer and aircraft observations.

As in the case of the meteorological analysis discussed in [section 3](#), statistics of background and analysis departures provide a basic metric of the quality of the aerosol assimilation. [Figure 12](#) shows probability distribution functions of collocated observation-minus-forecast and observation-minus-analysis departures from MERRA-2 for each sensor in the aerosol observing system. Statistics are shown in terms of the log-transform AOD analysis variable [i.e., $\ln(\text{AOD} + 0.01)$] which is approximately normally distributed ([Randles et al. 2017](#)). Note that AOD is a dimensionless quantity and log-transformed AOD is typically in the range ($-4, 2$). As

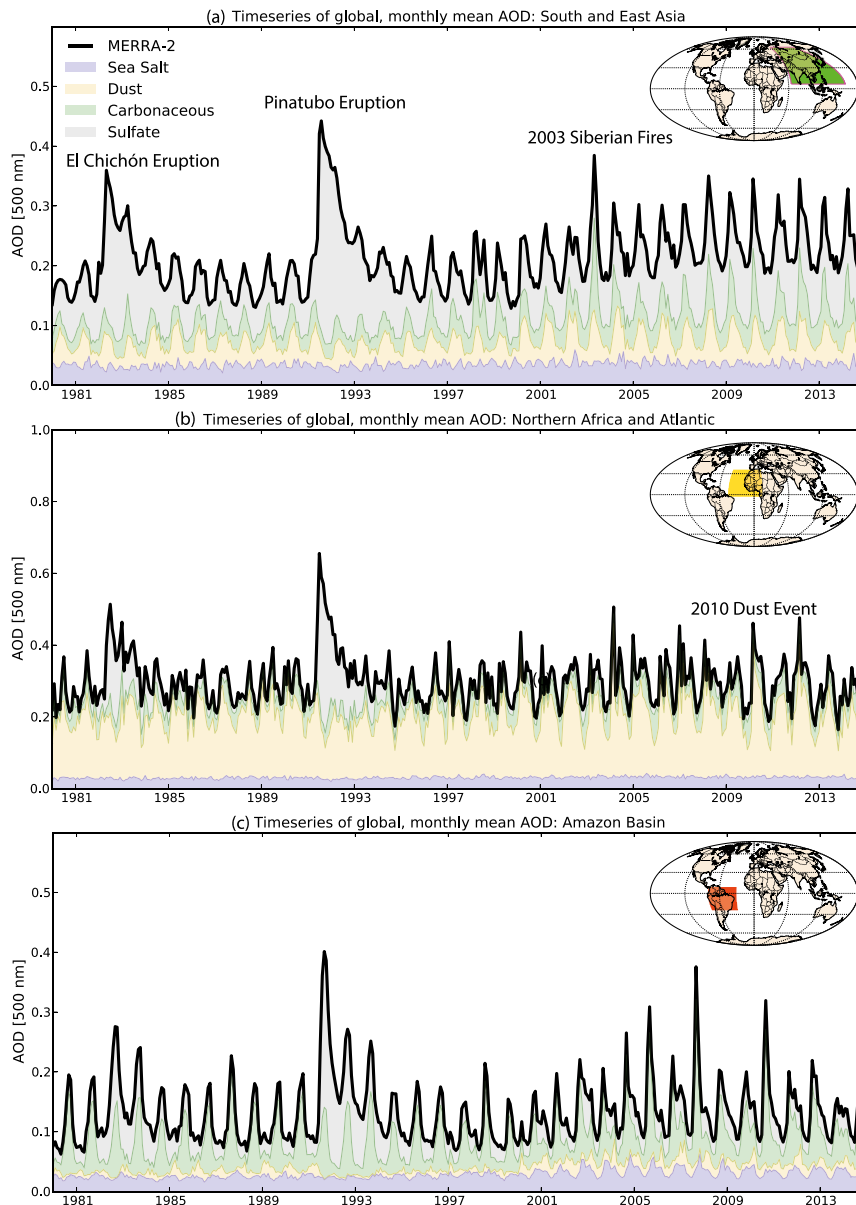


FIG. 13. Time series of area-weighted AOD from the MERRA-2 aerosol reanalysis averaged over major aerosol source regions: (a) South and East Asia (5° – 55° N, 65° – 160° W), (b) northern Africa (2.5° S– 30° N, 45° W– 15° E), and (c) the Amazon basin in South America (20° S– 7.5° N, 80° – 30° W). The total AOD (thick black line) is the sum of contributions from sea salt (blue), dust (yellow), carbonaceous (black) and organic carbon (green), and sulfate (gray) AOD. Results are derived from the data collection described in GMAO (2015g).

expected, compared to the forecast departures, the analysis departures show reduced bias with respect to the observations. Note also that the innovation variances are much larger over land than ocean, a direct consequence of the signal-to-noise limitation of aerosol retrievals over land.

Regional aspects of the global distribution of aerosols are illustrated in Fig. 13, which shows time series of

analyzed AOD from MERRA-2 area averaged over several major aerosol source regions. The contribution of each aerosol species to the total AOD is indicated by the colored shading. The seasonal cycles of dust and biomass burning (carbonaceous) AOD are apparent in all regions. Large increases in sulfate aerosol occur in all regions after the El Chichón (1982) and Mount Pinatubo (1991) volcanic eruptions. Over the Asian region (Fig. 13a),

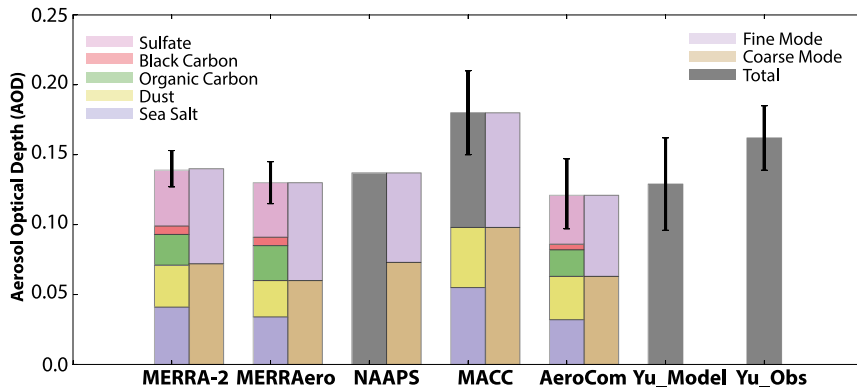


FIG. 14. AOD from aerosol reanalyses (MERRA-2, MERRAero, NAAPS, and MACC), intermodel comparisons (AeroCom phase I and Yu_Model), and observations (Yu_Obs) for the period 2003–10. Where available, total AOD is broken down by component species (left bar) and by fine and coarse mode (right bar). For MERRA-2 and MERRAero, the error bar represents the standard deviation of the monthly mean AOD for the period 2003–10. For MACC, the error bars are the uncertainty in the total AOD from Bellouin et al. (2013). AeroCom (Kinne et al. 2006) and Yu et al. (2006) uncertainty are the intermodel or observational standard deviations. Coarse mode is defined as the sum of dust plus sea salt AOD, with the remainder of the AOD assigned to the fine mode. Results for MERRA-2 are derived from the data collection described in GMAO (2015g).

the analysis captures high carbonaceous aerosol associated with the 2003 Siberian fires and the increasing trend in AOD between the late 1990s and present [commensurate with increasing anthropogenic aerosol emissions reported by Diehl et al. (2012)]. The AOD over northern Africa (Fig. 13b) is dominated by dust, and major dust transport events such as in 2010 are captured (see B17 for details). Carbonaceous aerosol from biomass burning in major source regions such as the Amazon basin are also well captured (Fig. 13c), especially after 2000, when emissions inventories derive from MODIS observations (Darmenov and da Silva 2015).

Figure 14 compares values of AOD from several recent aerosol reanalyses for the period 2003–10. Where such information is available, the results are partitioned by species and identified as either fine or coarse mode (see caption for details). Also shown are multimodel average results from phase I of AeroCom (Kinne et al. 2006), as well as both model (Yu_Model) and observational (Yu_Obs) estimates from Yu et al. (2006). The latter study includes an attempt to account for satellite clear-sky biases by combining MODIS and MISR observations with the GOCART model. Compared to MERRAero, for example, MERRA-2 has slightly higher global average AOD because of increased contributions from dust (related to the assimilation of MISR AOD over bright surfaces) and sea salt (related to changes in model physics). MERRA-2 and NAAPS show similar global average AOD, both for fine- and

coarse-mode aerosol. Models without assimilation (AeroCom and Yu_Model) underestimate global average AOD compared to both observational estimates (Yu_Obs) and the aerosol reanalyses. The MACC aerosol reanalysis has the highest global mean AOD (Bellouin et al. 2013), which is close to the MODIS-only value of 0.188 for the period 2003–10 (Yu et al. 2006). MACC also has more dust and sea salt aerosol compared to the other reanalyses, particularly over the ocean (not shown).

The direct aerosol impact on the radiative energy balance of Earth is dependent on the vertical distribution of aerosol scattering and absorption, which is not fully constrained by the vertically integrated AOD measurements that MERRA-2 assimilates. An assessment of the aerosol vertical structure and absorption is presented in a companion paper (B17). Long-term aerosol reanalyses can potentially reduce uncertainty in how aerosol direct effects have changed over time, particularly once better observational constraints on aerosol absorption become available. The DRE of all aerosols is defined as the flux difference (in W m^{-2}) between clear-sky and clear clean-sky conditions (no aerosols or clouds). In the absence of clouds, this quantity is less sensitive to the vertical distribution of aerosol absorption, although it remains sensitive to absorbing aerosols over surfaces with high albedo (Chylek and Coakley 1974).

Table 4 compares the DRE from MERRA-2, MERRAero, MACC, model intercomparisons, and the

TABLE 4. Clear-sky DRE from reanalyses and observations. Observed median and std dev from satellite-derived estimates in Yu et al. (2006), median and std dev from four global models in Yu et al. (2006), MERRA-2 and MERRAero climatological global area-weighted average (plus or minus monthly std dev) for 2003–10, and, for MACC, the 2003–10 global mean and uncertainty is given following Bellouin et al. (2013).

	Obs (Yu et al. 2006)	Models (Yu et al. 2006)	MERRA-2	MERRAero	MACC
Land-area avg					
AOD	0.225 ± 0.038	0.178 ± 0.029	0.180 ± 0.027	0.171 ± 0.030	0.203 ± 0.030
AAOD	—	—	0.012 ± 0.002	0.016 ± 0.003	0.010 ± 0.003
TOA DRE	-4.85 ± 0.45	-2.80 ± 1.19	-3.09 ± 0.62	-3.11 ± 0.70	-6.40 ± 1.00
SFC DRE	-11.70 ± 1.20	-7.20 ± 1.86	-8.35 ± 1.82	-8.64 ± 2.04	-11.50 ± 1.90
ATM DRE	6.85 ± 0.75	4.90 ± 0.81	5.26 ± 1.23	5.53 ± 1.37	5.10
Ocean-area avg					
AOD	0.138 ± 0.024	0.100 ± 0.042	0.123 ± 0.008	0.111 ± 0.010	0.170 ± 0.030
AAOD	—	—	0.005 ± 0.001	0.005 ± 0.001	0.007 ± 0.001
TOA DRE	-5.45 ± 0.70	-3.50 ± 1.28	-3.65 ± 0.21	-3.44 ± 0.24	-7.70 ± 1.50
SFC DRE	-8.80 ± 1.65	-4.80 ± 1.60	-5.74 ± 0.41	-5.58 ± 0.47	-10.60 ± 1.90
ATM DRE	3.60 ± 1.30	1.30 ± 0.72	2.09 ± 0.27	2.14 ± 0.29	2.90

observationally constrained estimate of Yu et al. (2006). Listed are the TOA, surface (SFC), and atmospheric (ATM) estimates of DRE for the period 2003–10, averaged over land and ocean separately. Note that the atmospheric contribution to the DRE is defined as the difference between top-of-the-atmosphere and surface values, ATM = TOA – SFC. Over land, the DRE estimate from MACC best agrees with the observationally constrained estimate. TOA and SFC forcing in MERRA-2 and MERRAero are lower than in MACC because of their lower AOD, although the atmospheric forcing is similar. Over ocean, the DRE estimates from MERRA-2 and MACC are lower and higher, respectively, than the observational estimate, and both reanalyses have lower estimates of atmospheric absorption. Much of the uncertainty in the DRE reported by the IPCC arises from differences between estimates from global models and satellite-based estimates (Myhre 2009). However, as aerosol reanalyses like MERRA-2 continue to mature and incorporate additional observations (e.g., from lidars and multispectral sensors), we expect a narrowing of the gap between simulated and satellite-based estimates of the DRE.

5. Precipitation

The representation of precipitation in a reanalysis is key to applications in weather and climate, as it ties together aspects of both the water and energy cycles. It also presents a significant challenge, however, as estimates of precipitation are only indirectly constrained by observations and are strongly dependent on model physics whose parameterizations have known errors and can be highly sensitive to even small changes in large-scale temperature and humidity fields. The observations themselves can sometimes introduce additional

uncertainty in these estimates as a result of heterogeneous sampling, changes in instrumentation, and time-varying calibration (Bosilovich et al. 2017).

While improved representation of the hydrological cycle was a primary focus of MERRA, the character of its global precipitation in particular was found to be highly sensitive to the assimilated observations and thus to changes in the observing system (e.g., Robertson et al. 2011). Among the development aspects of MERRA-2 intended to address this issue are modifications to GEOS to conserve atmospheric dry mass and ensure that changes in global atmospheric total mass are equivalent to changes in total water (section 2f), exclusion from the analysis of microwave temperature sounding channels with strong surface sensitivity (section 2d), and, less directly, forcing of the land surface by observation-corrected precipitation estimates (section 2g).

a. Global aspects

Bosilovich et al. (2015, 2017) have investigated the global water cycle variability in MERRA-2 using comparisons with observational datasets and other recent reanalyses. Those studies present a broad range of metrics on this topic, a small subset of which are summarized

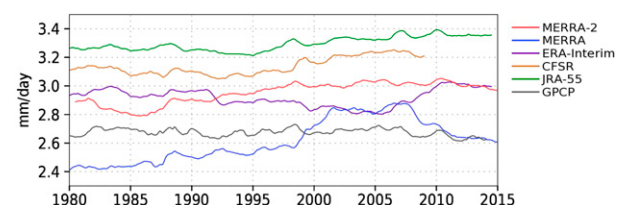


FIG. 15. Time series of 12-month running mean globally averaged precipitation (mm day^{-1}) for several reanalyses and the GPCP-merged gauge satellite data product. Results for MERRA-2 are derived from the data collection described in GMAO (2015h).

here. Figure 15 shows time series of global mean precipitation for several recent reanalyses and the observation-based estimates from GPCP (Adler et al. 2003). MERRA-2 exhibits larger temporal variability than GPCP but similar temporal variability to other recent reanalyses and noticeably less spurious temporal variability than MERRA. The largest improvements compared with MERRA in this regard relate to the decreased sensitivity of MERRA-2 to the introduction of AMSU-A radiances on *NOAA-15* and *NOAA-16* in the late 1990s, and to the loss of SSM/I radiances in the late 2000s. There is still an obvious sensitivity in MERRA-2 to the introduction of SSM/I in 1987, but the response to these data is comparable in magnitude to those of the other reanalyses shown. The response in MERRA-2 appears accentuated as a result of the decrease and subsequent recovery of precipitation through the mid-1980s. This behavior is not reflected in the GPCP time series but is evident to lesser degrees in CFSR and ERA-Interim, especially after 1983. For MERRA-2 and CFSR, this may be related to the fact that the SST boundary conditions used in these reanalyses reach their global minimum value for the entire reanalysis period after 1985 (Fig. 5), but further investigation is required to confirm this. The increasing trend in global precipitation in MERRA-2 from approximately 2.9 mm day^{-1} in 1988 to approximately 3.0 mm day^{-1} in 1998 is likely due to increasing evaporation over oceans driven by the assimilation of additional SSM/I wind speed observations and the tight coupling of evaporation and precipitation in MERRA-2 through the global mass constraint (Bosilovich et al. 2017). Overall, the global mean precipitation values are higher than those of GPCP but well within the envelope of other recent reanalyses.

Spatial comparisons provide additional insight into the strengths and weaknesses of the representation of precipitation globally in MERRA-2. Figure 16 shows maps of time-averaged differences in precipitation during boreal summer for MERRA and MERRA-2 compared with GPCP. MERRA-2 shows general improvement compared to MERRA over oceanic regions in both the tropics and extratropics, but an increase in positive bias over northern high latitudes. A notable deficiency in MERRA-2 is the excessive precipitation in the vicinity of high topography in the tropics, especially along the Andes and over the Maritime Continent. This is related to the partitioning between resolved (large scale) and parameterized (convective) precipitation in the MERRA-2 model, which, being more heavily skewed toward the former, results in large-scale precipitation over high topography that is difficult to control. In comparing these features with available gauge

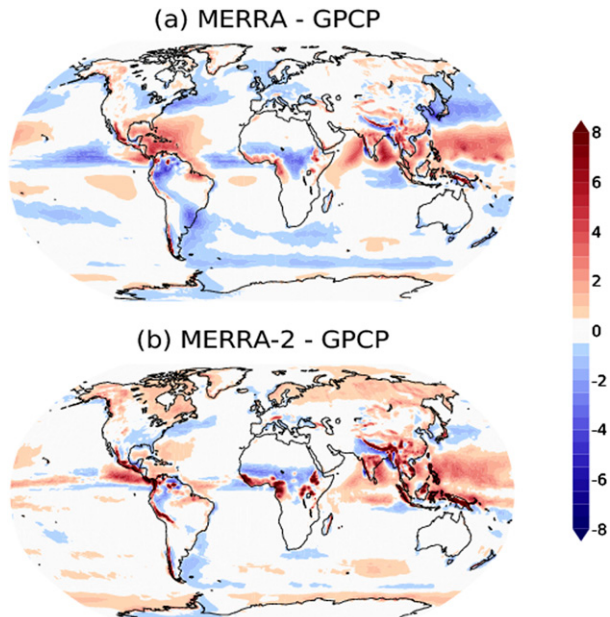


FIG. 16. Time-averaged precipitation differences (mm day^{-1}) during June–August for (a) MERRA minus GPCP and (b) MERRA-2 minus GPCP for the period 1980–2015. Results for MERRA-2 are derived from the data collection described in GMAO (2015h).

data, Bosilovich et al. (2015) point out that the maximum precipitation values in MERRA-2 do not always coincide with the maximum terrain height, so other effects also may play a role locally. Despite this deficiency over tropical land areas, the positive bias over the warm pool present in MERRA is slightly improved in MERRA-2. Additionally, the high precipitation bias over the Central American Seas in MERRA has been reduced significantly in MERRA-2, and precipitation over the Bay of Bengal and Arabian Sea is slightly improved. Results for other seasons (not shown) are qualitatively similar to those in Fig. 16.

b. U.S. summertime precipitation variability

Deficiencies in the ability of MERRA to reproduce certain aspects of the summertime seasonal precipitation over the United States have been well documented (Bosilovich 2013). In particular, MERRA was unable to produce seasonal highs and lows in regional precipitation that were similar to observations. For example, droughts and floods were only weakly reproduced.

Figure 17 shows the time series of summertime seasonal precipitation anomalies over the U.S. Midwest as derived from the NOAA CPC gauge observations and from MERRA and MERRA-2 model-generated precipitation. (The correlation values between various reanalyses and the gauge data for this and other regions of

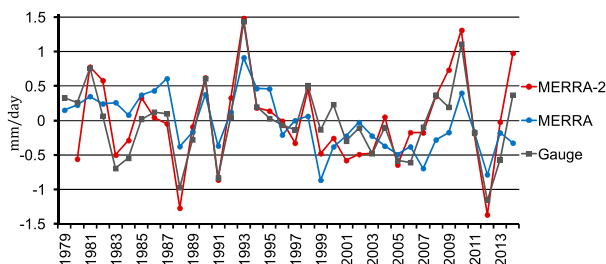


FIG. 17. Time series of Midwest summer seasonal precipitation anomalies (mm day^{-1}), following Bosilovich (2013). The anomalies are computed from the June–August mean for the period 1980–2011. The gauge data are from NOAA CPC gridded daily data for the United States (Xie et al. 2007). Results for MERRA-2 are derived from the data collection described in GMAO (2015h).

the United States are shown in Fig. 18.) The limitations of MERRA are apparent, especially when comparing values for 1988 (regional drought) and 1993 (large-scale flooding) with the observed values. In contrast, MERRA-2 is able to reproduce the 1988 and 1993 anomalies and is generally much better at tracking the overall variability of the observed anomalies. The poor performance of MERRA-2 in 1980 is a notable exception. A significant drought occurred in the southern Great Plains that year, but its location in MERRA-2 extended too far northeastward into the Midwest.

Figure 18 presents regional summary statistics for U.S. summer seasonal precipitation anomalies for selected reanalyses. The regions are defined as in Bosilovich (2013). For each region, the temporal mean, standard deviation, and anomaly correlation with respect to the CPC data are derived from time series like those shown in Fig. 17. In general, precipitation mean values across the United States are improved in MERRA-2 compared with MERRA (Fig. 18a), and in many regions the values for MERRA-2 improve over those of other reanalyses as well. There is also a marked increase in the standard deviation of the MERRA-2 time series relative to MERRA (Fig. 18b). As discussed above, for example, MERRA-2 more realistically reproduces the seasonal extremes in Midwest precipitation. Note, however, that MERRA-2 overestimates the standard deviation with respect to the CPC estimates in some regions. Ancillary results indicate that this is due to an excess in the number of days with rain in MERRA-2. Improvements in MERRA-2 are most evident in the anomaly correlation of the seasonal time series (Fig. 18c). In this measure, the two most recent reanalyses, JRA-55 and MERRA-2, generally outperform the others. MERRA-2 produces the highest correlations of the reanalyses shown in most regions, with substantially higher correlations in a few of these regions.

The detection and analysis of extreme weather, including extreme precipitation events, is a topic of

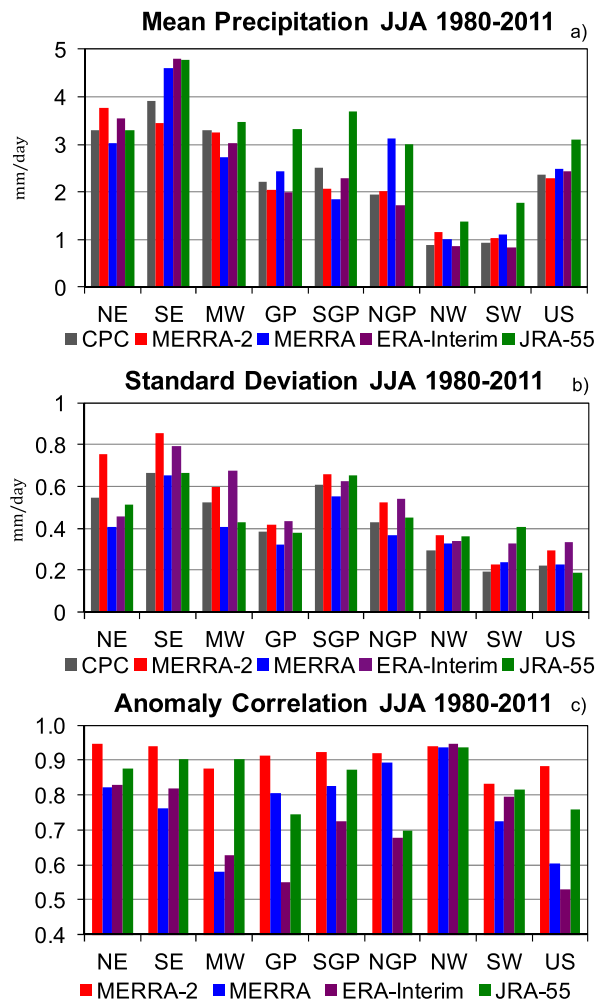


FIG. 18. Regional summary statistics for the U.S. summer seasonal anomaly time series of precipitation: (a) mean (mm day^{-1}), (b) standard deviation (mm day^{-1}), and (c) anomaly correlation to CPC gauge observations. The anomalies are computed from the June–August mean for the period 1980–2011. The regions lie within the continental United States and are defined as in Bosilovich (2013): Northeast (NE), Southeast (SE), Midwest (MW), Great Plains (GP), southern Great Plains (SGP), northern Great Plains (NGP), Northwest (NW), Southwest (SW), and the accumulation of all area in these regions (US). Results for MERRA-2 are derived from the data collection described in GMAO (2015h).

societal interest and another potential application of reanalyses. At least some of this interest is related to assessing changes in the risk of such events in the context of climate change. For example, observation-based studies cite strong evidence of an upward trend in the frequency and intensity of extreme precipitation events averaged over the United States during the last 50 years (Kunkel et al. 2013), although the causes of the observed trends are less certain. Figure 19 shows the accumulated precipitation amounts for the largest precipitation

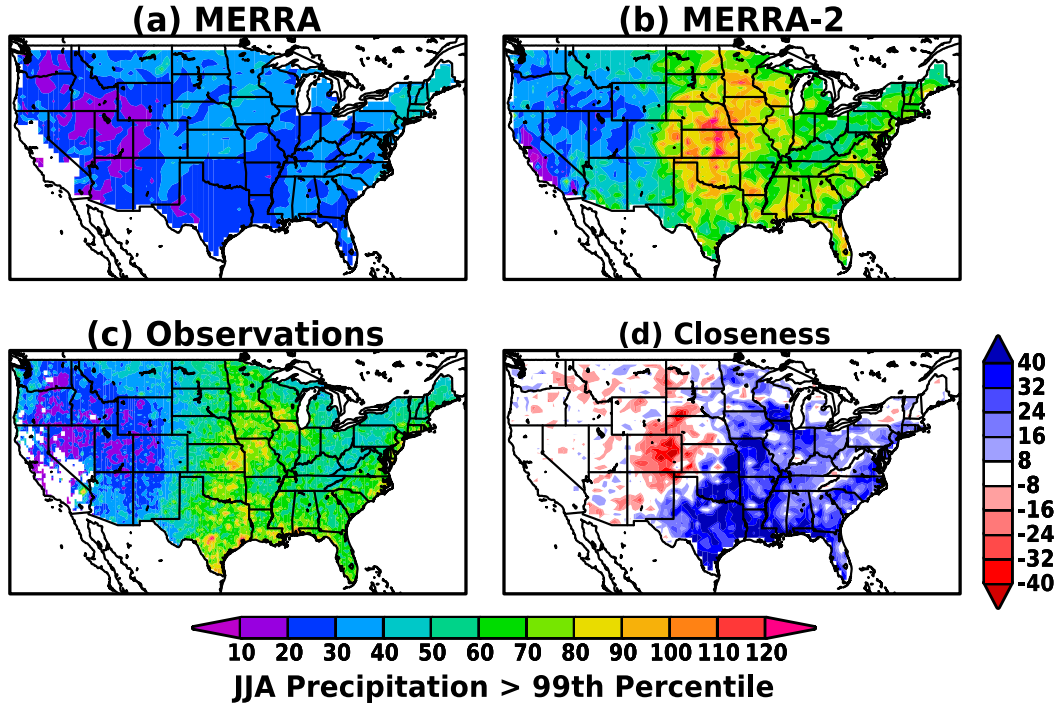


FIG. 19. Average amount of precipitation (mm day^{-1}) that exceeds the 99th percentile during June–August for the period 1980–2013 for (a) MERRA, (b) MERRA-2, and (c) CPC gauge observations. (d) The closeness of each reanalysis to the CPC observations for the same period (mm day^{-1}), defined as $|\text{MERRA-2} - \text{CPC}| - |\text{MERRA} - \text{CPC}|$, where the vertical bars indicate absolute differences and the names indicate the set of time-averaged gridpoint values for each data type. In (d), blue (red) shades indicate that MERRA-2 (MERRA) is closer to the CPC observations. Results for MERRA-2 are derived from the data collection described in [GMAO \(2015d\)](#).

events (at the 99th percentile) as derived from gauge observations, MERRA, and MERRA-2. Compared with the observations, MERRA shows very low values and very little structure across the continental United States. MERRA-2, on the other hand, exhibits a spatial pattern more similar to the observations, and the magnitude of the extreme rainfall is also more similar to the observations. MERRA-2 does, however, overestimate the precipitation values over the Midwest. While the results in Fig. 19 provide an indicator of how the representation of extreme events has improved in MERRA-2 compared with MERRA, the relatively coarse resolution of both reanalyses limits their utility for studying such events in detail. Presumably, the trend toward increasing resolution, among other improvements, will reduce these limitations in future global reanalyses.

6. The stratosphere

In MERRA-2 the stratospheric meteorology and ozone have benefited from improvements to the GEOS atmospheric model and GSI analysis scheme, as well as from the addition of observations that were not

incorporated into MERRA. The model changes most relevant to the stratosphere are the use of the cubed-sphere grid and the retuning of the GWD parameterization. The amplitude of the nonorographic GWD was increased in the tropics, enabling a model-generated QBO that was not found in the model version used for MERRA ([Molod et al. 2015](#)). Having a model-generated QBO, in turn, results in smaller lower-stratospheric analysis wind increments in MERRA-2 than in MERRA ([Coy et al. 2016](#)). The strength of the orographic GWD was also increased in the Southern Hemisphere to better model the strong, late-winter westerlies found there ([Molod et al. 2015](#)).

The main GSI change relevant to the stratosphere is the use in MERRA-2 of the CRTM for the assimilation of SSU radiances, while in MERRA the SSU assimilation was based on GLATOVS (section 2d). These SSU radiance channels are a major source of stratospheric information during the 1980s and 1990s, although the SSU instruments during these decades span several satellite platforms, each with different bias characteristics ([Kobayashi et al. 2009](#)). The CRTM has been enhanced for SSU data assimilation since MERRA and now accounts for these biasing factors.

The main additional observations relevant to the stratosphere for MERRA-2 are GPSRO bending angle observations from the suite of platforms beginning in July 2004 and temperature and ozone measurements of the middle atmosphere from MLS and OMI on the EOS *Aura* satellite beginning later the same year (Froidevaux et al. 2006; Schwartz et al. 2008; McPeters et al. 2008). MERRA-2 assimilates GPSRO bending angle observations up to 30 km. Details of the GPSRO platforms assimilated by MERRA-2 can be found in McCarty et al. (2016). The GPSRO observations aid lower-stratospheric bias correction by providing a stable source of temperature and moisture measurements. The MLS-retrieved temperature profiles are assimilated in MERRA-2 at altitudes above 5 hPa, providing a strong constraint on the dynamics of the stratopause and lower mesosphere. As shown below in section 6a, this improves the quality of the synoptic meteorological fields at these altitudes but may complicate the study of trends. The MLS and OMI contributions to ozone assimilation are discussed in section 6b.

a. Meteorology

The cubed-sphere discretization of the MERRA-2 model eliminates computational instabilities near the poles, a characteristic of latitude-longitude grids. This is especially important for stratospheric analysis where strong cross-polar flow events occur frequently, especially during major sudden warming events, as planetary-scale Rossby waves disturb the polar vortex. Ertel's potential vorticity (EPV), a scalar based on the horizontal vorticity, is often used to characterize the stratospheric circulation (Andrews et al. 1987), where stronger EPV gradients imply stronger flow. Figure 20 illustrates a case where the analyzed wind speeds in MERRA-2 reached nearly 170 m s^{-1} close to the polar stratopause at 1200 UTC 2 January 1995. On a global scale (Figs. 20a,b), the MERRA and MERRA-2 EPV fields appear similar, with the polar vortex (indicated by green and orange colors) displaced well off the pole. In both cases, strong winds cross the North Pole as they circle around the region of high EPV. However, a closer look reveals that the EPV in MERRA (Fig. 20c) has anomalous radial perturbations near the pole, while the EPV in MERRA-2 (Fig. 20d) shows a smooth and strong EPV gradient in this region. Note also that, while the largest discontinuities in the MERRA EPV field occur close to the pole itself, their effects can extend well beyond this location.

Figure 21 provides an example of how the assimilation of MLS temperature measurements in MERRA-2 improves the representation of the dynamics near the stratopause. The figure shows the time-height evolution

of polar temperatures during the 2005/06 Northern Hemisphere winter in which a major stratospheric sudden warming occurred. In a comprehensive study of this winter based on MLS observations, Manney et al. (2008) documented the disappearance of the warm polar stratopause during the warming and its later high-altitude reformation and subsequent descent. This breakdown and high-altitude reformation in early February 2006 is now well captured in MERRA-2 (Fig. 21b), in contrast to MERRA (Fig. 21a).

The characteristics of the assimilation on longer time scales is illustrated in Fig. 22, which shows the time-height evolution of global monthly averaged temperature anomalies in MERRA-2. The 35-yr mean and annual cycle for the period 1980–2015 have been subtracted from each pressure level. The global temperatures in the lower stratosphere (100–10 hPa) show no obvious discontinuities as different instruments become available. There is a slight cooling with time over the 35 years, which is generally consistent with recent analyses of the satellite-based stratospheric climate data record [see Seidel et al. (2016) and references therein]. There are also episodic temperature increases associated with the two large volcanic eruptions, El Chichón in 1982 and Mount Pinatubo in 1991. In the upper stratosphere, several discontinuities can be seen. There is a marked decrease in temperature near 1 hPa in 1995 when the transition from assimilating NOAA-11 through NOAA-14 SSU channel 3 radiances occurs. The latter are demonstrably cooler [see Fig. 16 of McCarty et al. (2016)] and are assimilated without bias correction because of the relatively large model errors at this level. There is an overall increase in temperature when AMSU-A data are first assimilated in 1998, which was not as apparent in MERRA (Rienecker et al. 2011) because of using overlapping SSU channel 3 and AMSU-A channel 14 radiances in that reanalysis. The overall effect of assimilating the MLS temperature profiles beginning in 2004 is to sharpen the stratopause with warming at approximately 1 hPa and cooling above and below this level.

b. Ozone

The most notable aspects of the MERRA-2 ozone analysis, and those that constitute the main differences with MERRA, are the use of the improved version of SBUV data prior to October 2004 and subsequent assimilation of OMI and MLS observations. The latter provides high-vertical-resolution ($\sim 2.5 \text{ km}$) measurements of stratospheric ozone profiles during both night and day. The specification of background errors for ozone has also been upgraded to account for flow-dependent error standard deviations, as described in Wargan et al. (2015).

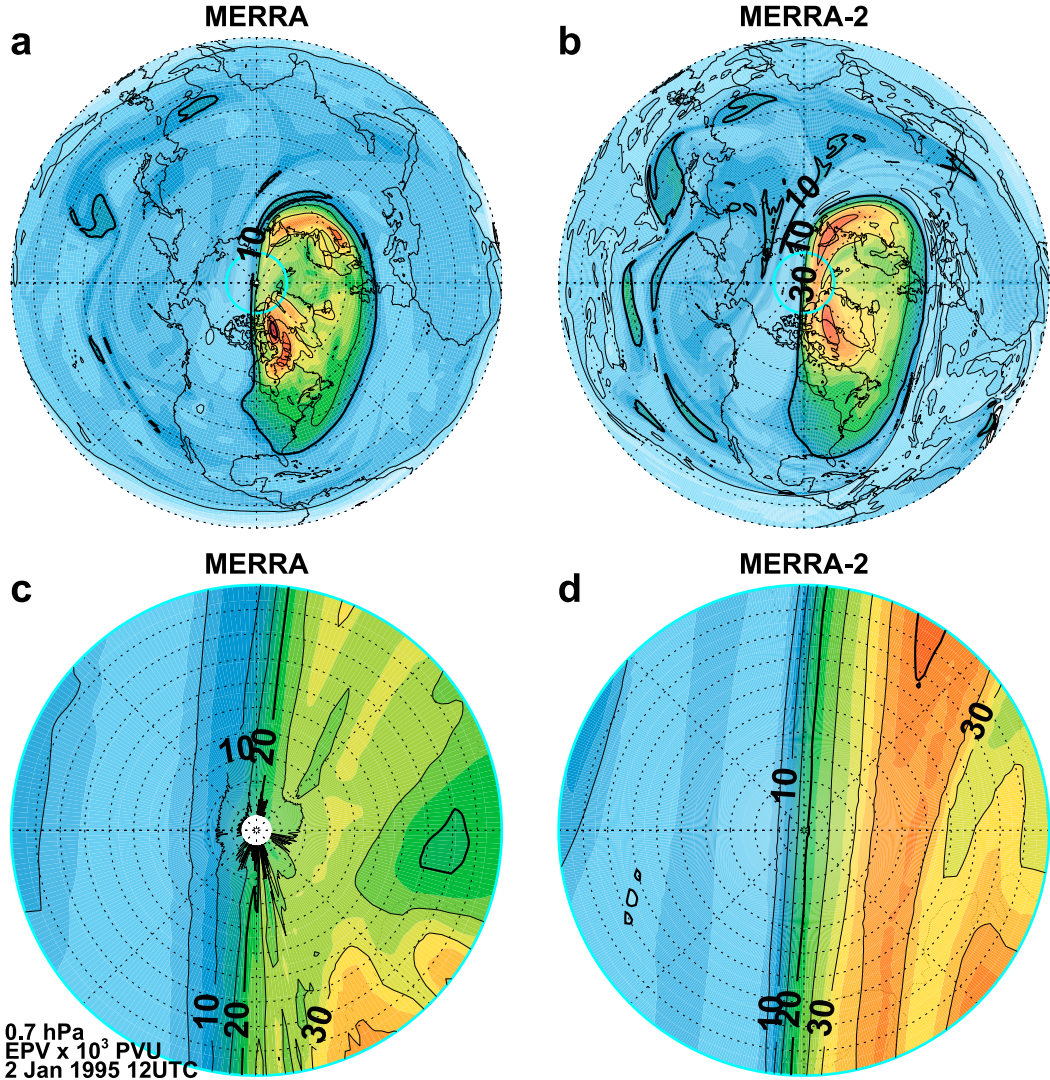


FIG. 20. EPV [10^3 potential vorticity units (PVU; $1 \text{ PVU} = 10^{-6} \text{ m}^{-2} \text{ s}^{-1} \text{ K kg}^{-1}$)] at 0.7 hPa at 1200 UTC 2 Jan 1995 for (a) MERRA and (b) MERRA-2 for the Northern Hemisphere. Polar cap detail (80° – 90°N) for (c) MERRA and (d) MERRA-2. Color shading interval is 2.5×10^3 PVU. Black contour interval is 10×10^3 PVU in (a) and (b) and 5×10^3 PVU in (c) and (d). Cyan circle denotes 80°N . Results are derived from the data collection described in GMAO (2015c).

Many ozone datasets exist for various periods between 1980 and the present. The decision to use only SBUV, MLS, and OMI observations in MERRA-2 was motivated by the desire to avoid introducing multiple discontinuities into the ozone observing system while taking advantage of high-quality data offered by SBUV and EOS *Aura* retrievals. This approach leads to a relatively homogeneous MERRA-2 ozone record with only one major discontinuity in 2004 when MLS and OMI data replace SBUV observations. The price is a degraded quality of the analyzed ozone during the short periods when the selected data are not available, most notably in the Southern Hemisphere in late 1994, as discussed below.

An initial evaluation of the representation of ozone in MERRA-2 was presented in Bosilovich et al. (2015). A more comprehensive validation against independent satellite and ozonesonde data, including evaluation of the vertical structure and variability, is given in Wargan et al. (2017). In particular, it is shown there that the assimilation of MLS observations in MERRA-2 leads to significant improvements in the representation of lower-stratospheric ozone when compared with MERRA or compared with the period of SBUV assimilation in MERRA-2. The QBO signal in ozone is discussed by Coy et al. (2016), who demonstrate an improvement in the vertical structure of the ozone QBO signature from

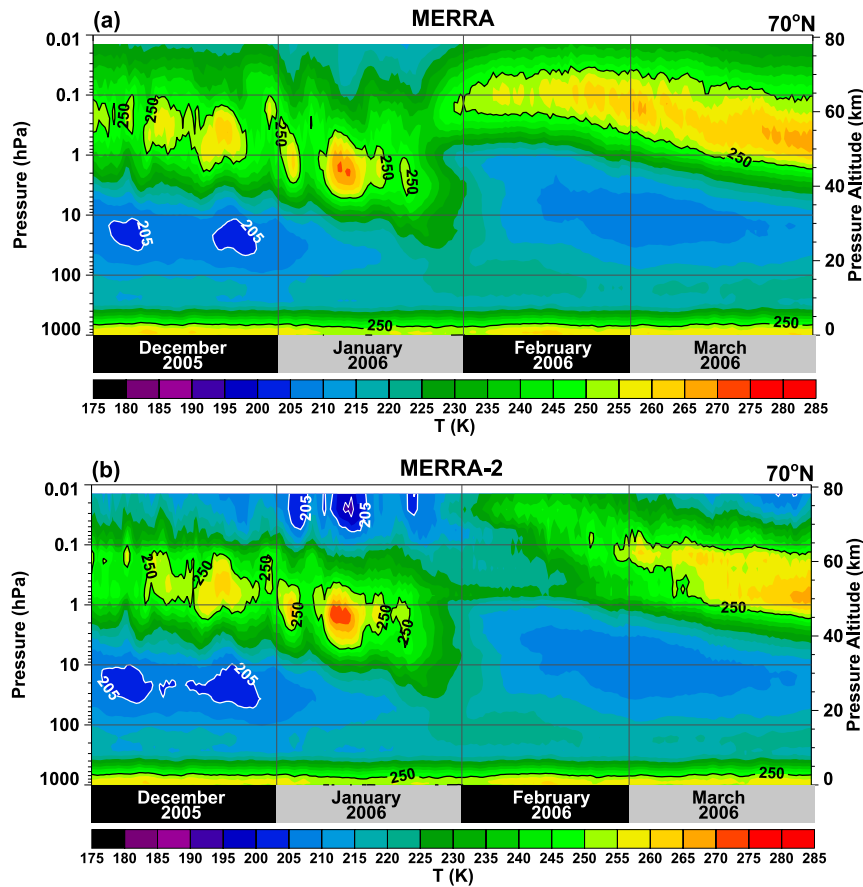


FIG. 21. Time–altitude section of zonally averaged temperature at 70°N for (a) MERRA and (b) MERRA-2. The time resolution is twice daily (0000 and 1200 UTC) for December 2005–March 2006. The contour interval is 5 K.

2004 onward, when MLS data are assimilated in MERRA-2. The focus here is on the Antarctic total column ozone in order to illustrate that MERRA-2 has realistic climatic ozone in a poorly observed region, while also highlighting some of its uncertainties. Two examples are presented: a comparative evaluation of the South Pole ozone in MERRA and MERRA-2 and the representation of Antarctic ozone holes in the present reanalysis. The former follows Wargan et al. (2017).

Figure 23a shows the time series of total ozone derived from ozonesonde measurements at the South Pole, along with MERRA and MERRA-2 output sampled at the ozonesonde times and location between 1986 and 2015. The ozonesonde data, including the integrated column values, were obtained from the Earth System Research Laboratory website (<http://www.esrl.noaa.gov/gmd/ozwv/ozsondes/spo.html>). Note that the vertical range of balloonborne measurements typically does not extend to pressure levels above 10 hPa, so the upper-stratospheric portion of the column is obtained by extrapolating the mixing ratios from 7 hPa or from the

highest observed altitude, whichever is lower. For completeness, Fig. 23a also shows the reanalysis data between 1980 and 1985. In the absence of ozonesondes, the reanalyses are sampled four times monthly in one-week intervals for that period. The differences between each reanalysis and the ozonesonde values are plotted in Fig. 23b. Overall, both reanalyses capture the annual cycle and much of the interannual variability observed in the ozonesonde data, although there are large discrepancies (greater than 50%) during austral summer months in MERRA-2 prior to 2005 and in MERRA throughout the period of comparison. This is consistent with the fact that the reanalyses are not constrained by SBUV data during polar night. In addition, in late 1994, the SBUV coverage was limited to latitudes north of approximately 30°S, owing to an orbital drift of the NOAA-11 satellite, which left the middle and high southern latitudes unobserved in both reanalyses. Nonetheless, these differences are reduced in MERRA-2 compared to MERRA. MERRA-2 performs significantly better than MERRA relative to the South Pole

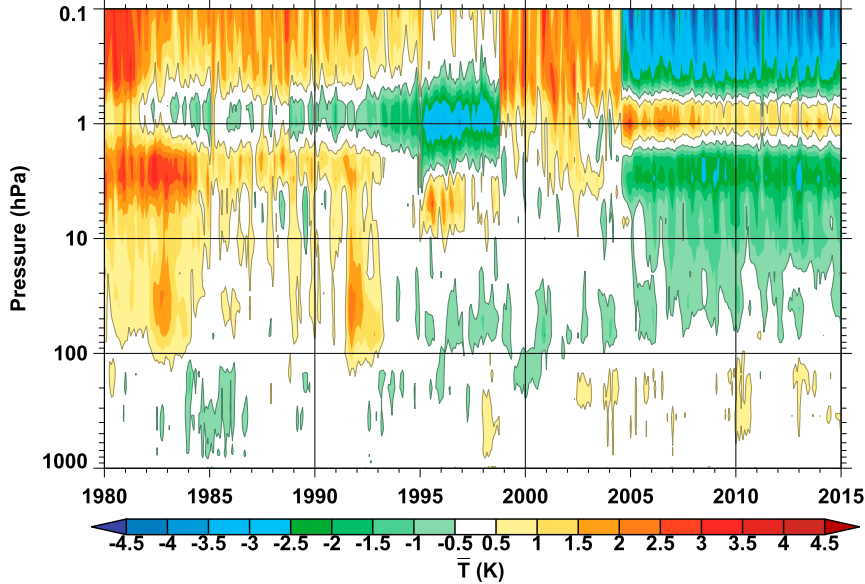


FIG. 22. Monthly and globally averaged temperature anomaly for MERRA-2 as a function of time. The annual cycle and mean for 1980–2015 have been removed. The MLS temperatures were introduced at levels above 5 hPa beginning in August 2004. Results are derived from the data collection described in GMAO (2015c).

ozonesondes from October 2004 onward, when EOS *Aura* ozone data are assimilated. In particular, the standard deviation of the differences between MERRA-2 and the ozonesonde values drops from 12.5% between

1991 and 2004 to 5% between 2005 and 2014. At the same time, the correlation between MERRA-2 and the ozonesonde measurements increases from 0.88 to 0.98. The large excursions seen in Fig. 23b in MERRA

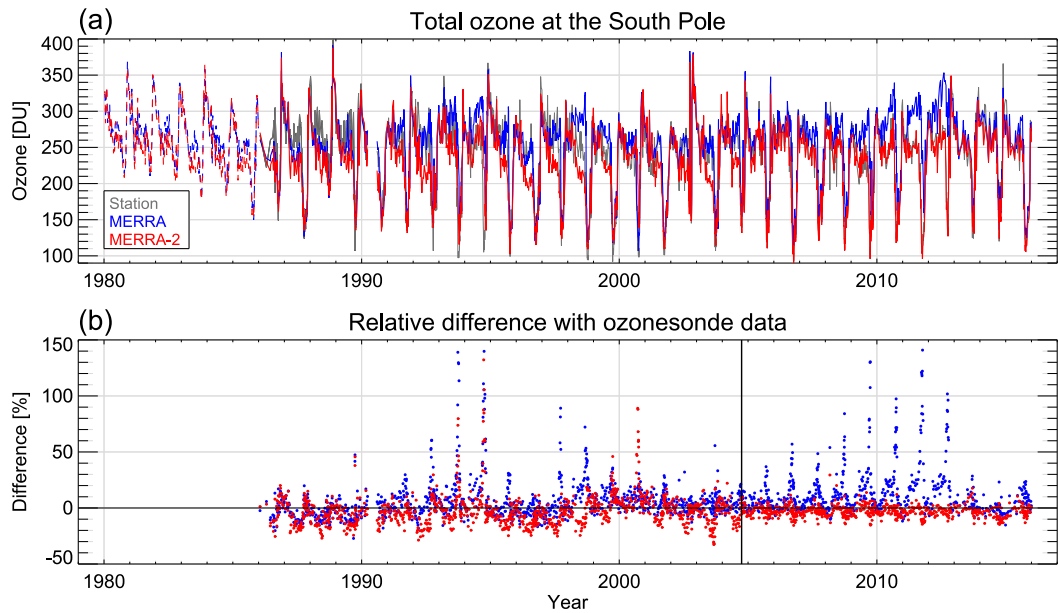


FIG. 23. Time series of (a) total ozone (DU) at the South Pole derived from individual ozonesonde measurements (gray) and from collocated values in MERRA (blue) and MERRA-2 (red). Note that ozonesonde measurements are unavailable prior to 1986 (see text for details). (b) The reanalysis-minus-ozonesonde differences divided by sonde total ozone for MERRA (blue) and MERRA-2 (red). The black vertical line in (b) separates the SBUV and *Aura* periods. [Figure is from Wargan et al. (2017).] Results for MERRA-2 are derived from the data collection described in GMAO (2015a).

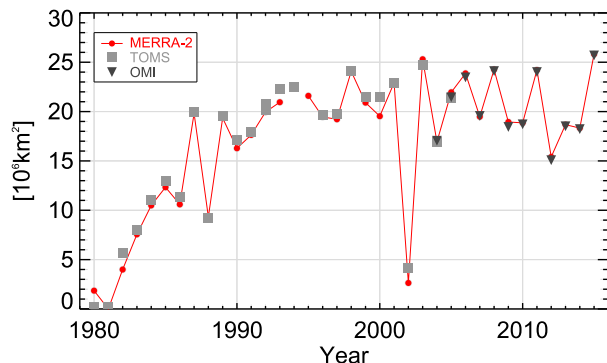


FIG. 24. Time series of the Antarctic ozone hole area (10^6 km^2) calculated from MERRA-2 ozone fields averaged between 20 Sep and 10 Oct for 1980–2015 (red curve with circles). Also shown are values derived from TOMS (gray squares) and OMI (black triangles) observations. Results for MERRA-2 in 1994 are excluded because of insufficient SBUV data coverage in the Southern Hemisphere, which significantly degraded the analysis (see text for details). Results for MERRA-2 are derived from the data collection described in GMAO (2015a).

between 2008 and 2012 are due to degraded coverage of the *NOAA-17* SBUV instrument. In contrast, the behavior of the MERRA-2 South Pole ozone is remarkably steady relative to the ozonesondes in the period when MLS and OMI data are assimilated. Only small seasonal variations are seen during that period. The MERRA-2 South Pole total ozone exhibits a small negative bias of approximately 6.7 Dobson units (DU), or roughly 2%, throughout the period of comparison. This bias does not vary significantly between the periods when either SBUV or EOS *Aura* ozone data are assimilated.

As discovered by Molina and Rowland (1974), anthropogenic emissions of chlorofluorocarbons provide the main contribution to the chlorine loading in the stratosphere, leading to destruction of the ozone layer. One prominent feature of the ozone loss in recent decades is the occurrence of springtime ozone holes over Antarctica since the early 1980s (Farman et al. 1985). Ozone holes are regions of extremely low values of total ozone forming inside the polar vortex as a result of a series of chlorine-catalyzed reactions (WMO 2014). The climatological importance of this phenomenon warrants its accurate representation in long-term reanalyses. The discussion here focuses on only one simple diagnostic, the ozone hole area, defined as the region with total ozone values less than 220 DU.

Figure 24 shows the time series of the ozone hole area calculated from the MERRA-2 total ozone averaged between 20 September and 10 October in each year between 1980 and 2015. Also plotted in Fig. 24 are the ozone hole area values derived from the TOMS instruments on *Nimbus-7* (1980–92), *Meteor-3* (1992–94),

and *Earth Probe* (1996–2005) and from OMI (2004–15). Note that OMI data are assimilated in MERRA-2, but TOMS observations are not. With the exception of 1994 there is remarkable agreement between MERRA-2 and these observations. In particular, MERRA-2 realistically captures the ozone hole interannual variability throughout the period of the reanalysis. There is an upward trend between 1980 and the mid-1990s followed by a plateau, with the area oscillating around $22 \times 10^6 \text{ km}^2$. This is consistent with the late-twentieth-century increase of anthropogenic chlorine and bromine loadings and the subsequent slow recovery after the gradual implementation of the Montreal Protocol of 1986 (WMO 2014). The protocol, which went into effect in the late 1990s, banned the release of the main ozone-depleting substances. Because the rate of the springtime polar ozone depletion depends on temperature and the strength of the Antarctic polar vortex in a given year, the size of the ozone hole exhibits a dynamically driven interannual variability superimposed on decadal-scale trends. This dynamical modulation is also evident in Fig. 24. The extremely small (less than $3 \times 10^6 \text{ km}^2$) ozone hole in 2002 occurred in conjunction with the only major sudden stratospheric warming in the Southern Hemisphere on record (Newman and Nash 2005).

It should be noted that the southern high-latitude ozone for 1994 in MERRA-2 is not recommended for scientific use. The degraded result for that year is due to limited SBUV data coverage, as explained above, and the decision not to use data sources other than SBUV, OMI, and MLS throughout the reanalysis. This particular deficiency is not shared with other major reanalyses (except MERRA), which replaced the missing data with other available observations, such as from the short-lived *Meteor-3* TOMS (ERA-Interim) or *NOAA-9* SBUV (CFSR and JRA-55) instrument data. The latter were not considered in MERRA-2 because of the poorer quality of its partial columns compared to other SBUV instruments.

Realistic ozone hole interannual variability is also present in MERRA (S. M. Davis 2016, personal communication) with the exception of 1993, 1994 (as in MERRA-2), and the period between 2010 and 2012 when poor coverage from *NOAA-17* SBUV resulted in degraded quality of the Antarctic ozone. The inferior performance of MERRA in 1993 compared to MERRA-2 is a consequence of applying more stringent data quality criteria to the older version of the SBUV data, resulting in limited data coverage near the terminator.

7. Representation of the cryosphere

Reanalyses provide a global context for assessing recent, pronounced high-latitude climate variability and

provide seamless information on linkages to lower latitudes. As compared to midlatitudes, reanalyses in polar regions are particularly challenged by the paucity of the in situ observational network, by the difficulty of satellite microwave and infrared sensors to profile the lower atmosphere over snow and ice surfaces, and by an inadequate representation of physical processes in models that are specific to these areas. Of these three challenges, improvement of model representations of physical processes—particularly as they relate to ice and snow surfaces—was seen as the most tractable in the development of MERRA-2.

Several changes in the representation of physical processes between MERRA and MERRA-2 are directly relevant to polar regions. These include the use in MERRA-2 of the cubed-sphere computational grid (e.g., Putman and Lin 2007), which removes the need for gravity wave filtering at high latitudes, as well as daily SIC and SST boundary conditions (Donlon et al. 2012; Reynolds et al. 2007; Taylor et al. 2000), as compared with the weekly fields used in MERRA.

In MERRA, a fixed surface albedo of 0.6 was used with sea ice cover. This resulted in erroneously warm surface temperatures in the Arctic spring, when the observed albedo is typically much higher (Cullather and Bosilovich 2012). In MERRA-2, Northern Hemisphere sea ice albedo varies seasonally based on flux tower observations from the SHEBA field experiment (Duynkerke and de Roode 2001). Monthly values are computed and then linearly interpolated in time to produce instantaneous values. Sea ice albedo in the Southern Hemisphere remains fixed as in MERRA, as there are few reliable albedo observations there. Sea ice in the Southern Hemisphere also does not endure an extended period of surface melting and a resulting decreased albedo as in the Northern Hemisphere. Comparisons with SHEBA observations indicate a substantial reduction in 2-m air temperature biases during boreal spring in MERRA-2.

These comparisons also find a warm bias in winter months over sea ice in MERRA-2 of approximately 1.2°C in comparison to SHEBA. Larger air temperature differences of greater than 3°C are found in comparison to Soviet ice drifting station observations made during the 1980s (Colony et al. 1992). Simmons et al. (2016) showed that MERRA-2 is an outlier in near-surface temperature trends in polar regions, as compared to ERA-Interim, JRA-55, and several conventional datasets. For the period 1980–2009, annual 2-m air temperatures for the North Polar cap bounded by 60°N increased by $0.35^{\circ} \pm 0.08^{\circ}\text{C decade}^{-1}$ in MERRA-2. This is the trend determined from linear

regression; the uncertainty denotes the standard error of the trend. By comparison, North Polar cap temperatures increased by $0.46^{\circ} \pm 0.09^{\circ}\text{C decade}^{-1}$ in NOAA CFSR, by $0.55^{\circ} \pm 0.10^{\circ}\text{C decade}^{-1}$ in ERA-Interim, and by $0.56^{\circ} \pm 0.09^{\circ}\text{C decade}^{-1}$ in JRA-55. The behavior in MERRA-2 may be attributable to spurious changes in the SST and SIC boundary conditions and the response of the model to changes in surface forcing. Investigation of these issues is ongoing.

A particular focus during the development of MERRA-2 was on the representation of glaciated land surfaces (Cullather et al. 2014). In MERRA, ice sheets had an unrealistic design, with a fixed surface albedo and no representation of surface hydrology. Surface energy fluxes were computed using a fixed subsurface temperature of 230 K (-43°C). In MERRA-2, energy conduction properties of the upper 15 m of ice are represented, as well as the energy and hydrologic properties of an overlying, variable snow cover. Snow hydrology follows a modified version of the Stieglitz model that is also used over terrestrial land surfaces (Lynch-Stieglitz 1994; Stieglitz et al. 2001). This provides an explicit representation of snow densification, meltwater runoff, percolation, refreezing, and a prognostic surface albedo based on Grewell and Konzelmann (1994).

Figure 25 shows the effects of the different surface configurations in MERRA and MERRA-2 on near-surface air temperatures over ice sheets. In MERRA, biases are found when the observed surface temperature differs markedly from the fixed subsurface temperature of -43°C . This includes South Pole station in winter (Fig. 25a), where MERRA values are more than 5 K too warm; over the central Ross Ice Shelf in summer (Fig. 25b), where MERRA is 8 K too cold; and over central Greenland in summer (Fig. 25c), where MERRA is 4 K too cold. It may be seen from Fig. 25 that these seasonal air temperature differences between MERRA and the station values are significant over interannual time periods. In contrast, 2-m air temperatures for these locations in MERRA-2 more closely agree with the observed values.

The surface representation in MERRA-2 also allows for the computation of surface mass balance over ice sheets, which may be defined as the net of precipitation minus evaporation minus runoff. The MERRA system does not provide runoff over land ice and, as seen in Fig. 26, lacks ablation areas (in which the annual surface mass balance is negative) along the periphery of the ice sheet. For Greenland these occur mostly as a result of runoff from surface melt. The corresponding fields in MERRA-2, on the other hand, compare well with those

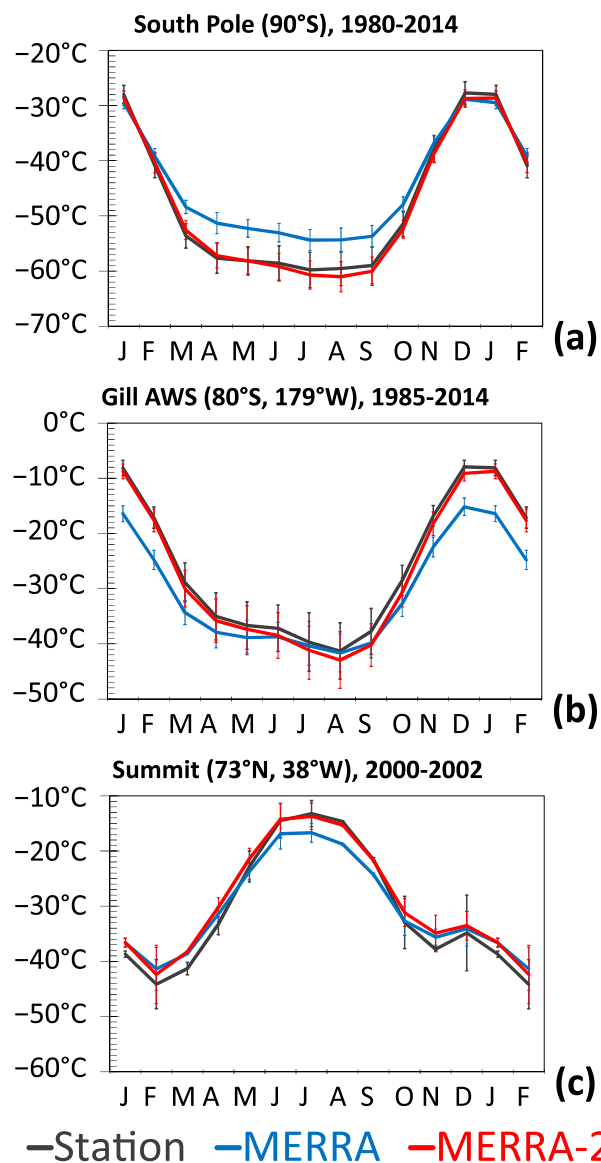


FIG. 25. Average annual cycle of 2-m air temperature ($^{\circ}$ C) in MERRA and MERRA-2 at (a) South Pole station [90 $^{\circ}$ S; 1980–2014 (Turner et al. 2004)], (b) Gill automatic weather station [80 $^{\circ}$ S, 179 $^{\circ}$ W; 1985–2014 (Turner et al. 2004)], and (c) Summit, Greenland [73 $^{\circ}$ N, 38 $^{\circ}$ W; 2000–02 (Hoch 2005)]. Vertical bars denote plus or minus one standard deviation of the multiyear time series for each month. Results for MERRA-2 are derived from the data collections described in GMAO (2015i,j,m).

from the widely used regional climate model MAR (Fettweis 2007), particularly in terms of the accumulation distribution in southeastern and western Greenland and the location of the zero-contour line along the western coast. However, some differences are also evident. For example, the regional climate model indicates average annual mean ablation values of up to 4 m yr^{-1} in southwestern Greenland, as compared with values

of approximately 1 m yr^{-1} in MERRA-2. In addition to differing surface representations, differences in grid spacing between MAR (25 km) and MERRA-2 (roughly 50 km) may also play a role. A final point of comparison in Fig. 26 is with regard to topography. The MERRA system used a dated topography, which contained large errors of up to 600 m over the Greenland Ice Sheet (Box and Rinke 2003). These differences are apparent in the topography contours shown for MERRA and MERRA-2 in Fig. 26.

8. MERRA-2 products and access

The complete list of analyzed and diagnosed fields produced by MERRA-2 is given in the product file specification document available at the GMAO's MERRA-2 website (<https://gmao.gsfc.nasa.gov/pubs/docs/Bosilovich785.pdf>) (Bosilovich et al. 2016). The GEOS IAU procedure allows for higher-frequency products than just the 6-hourly ones generated directly from the analysis. There are three time-invariant and 39 time-varying product collections, all produced on a $0.625^{\circ} \times 0.5^{\circ}$ horizontal grid. Variables are provided on either the native vertical grid (at 72 model layers or the 73 edges) or interpolated to 42 standard pressure levels. Detailed information and a description of each variable are available in the MERRA-2 file specification document. As in MERRA, MERRA-2 provides closed atmospheric budgets, including the analysis increment terms. The observational forcing from the assimilation increments during the IAU segment is summed in the output budgets of the model. Bosilovich et al. (2015) show the magnitudes of these terms in water and energy budgets.

The NASA GES DISC provides access to MERRA-2 products through a new unified user interface connected to three different search engines. Many of the tools will be familiar to MERRA users, such as the popular Giovanni visualization and analysis tool, web-based FTP servers and Open-Source Project for a Network Data Access Protocol (OpenDAP) web services. The subsetting capability has been updated to include grid transformation options, while retaining the essential functionality of selecting levels, variables, time, and domain. Citations for the individual MERRA-2 data collections are included in the GES DISC MERRA-2 data access pages. As noted in section 1, these citations are included in the figure captions of this paper (except where results for MERRA-2 are derived from other sources, such as diagnostic output from the data assimilation scheme). Results shown for MERRA are from similarly named data collections, as described by Rienecker et al. (2011).

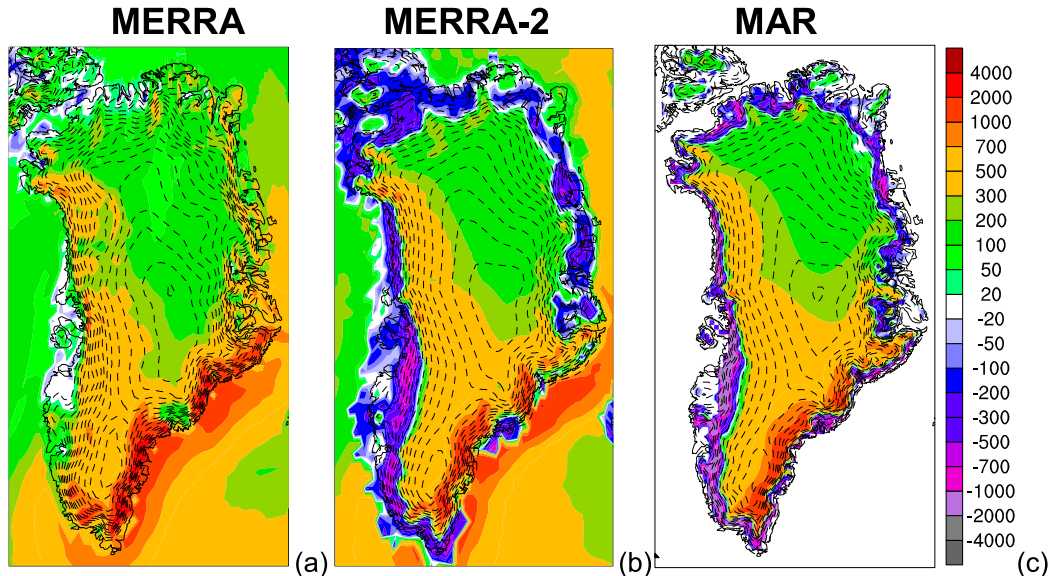


FIG. 26. Surface mass balance (mm yr^{-1} , water equivalent) for the Greenland Ice Sheet for the period 1980–2012 in (a) MERRA, (b) MERRA-2, and (c) MAR (Fettweis 2007). Surface topography (including ice sheet) is contoured with dashed lines every 200 m. Results for MERRA-2 are derived from the data collections described in GMAO (2015i,j,m).

9. Summary and outlook

The Modern-Era Retrospective Analysis for Research Applications, version 2 (MERRA-2), was developed with two primary objectives: to provide an ongoing near-real-time climate analysis of the satellite era that addresses known limitations of the now-completed MERRA reanalysis (January 1979–February 2016) and to demonstrate progress toward development of a future IESA capability. MERRA-2 has achieved those objectives in several respects. These include the assimilation of satellite observations not available to MERRA—which assimilated no new satellite observations after *NOAA-18* (launched in 2005)—the reduction of certain biases and imbalances in the water cycle, and the reduction of spurious trends and jumps in precipitation related to changes in the observing system. As a step toward a future IESA, MERRA-2 includes aerosol data assimilation and improved representations of aspects of the cryosphere and stratosphere, including ozone, as compared with MERRA.

At the same time, because of the fairly rapid development schedule required to produce a timely replacement for MERRA, other aspects of the MERRA-2 development received less attention. For example, there was little focus on the preparation and improvement of input conventional data types and minimal tuning of the model physics for the current application. Notable shortcomings of MERRA-2 compared with MERRA include an increased warm bias in the upper troposphere—as

revealed by the background forecast fit to radiosonde temperature observations and mean analysis increments of temperature—as well as excessive precipitation over high topography in the tropics and, to a lesser extent, over northern high latitudes. Subsequent experimentation indicates that these behaviors are most affected by the model parameterizations of deep convection and gravity wave drag in GEOS, as well as the representation of topography. They are being addressed in more recent model versions.

Ongoing development in other aspects of modeling and data assimilation are likely to provide benefit for reanalyses in the near future. For example, while MERRA-2 assimilates only clear-sky satellite radiances, the use of cloud- and rain-affected radiances—referred to as all-sky assimilation (Bauer et al. 2010)—has matured or become operational at several centers including GMAO. This should improve the assimilation of moisture-sensitive data types, which, as shown here and by Bosilovich et al. (2017), can still induce unexpected changes in global precipitation and moisture fields. Direct assimilation of land surface observations, including remotely sensed soil moisture and snow cover fraction, is another area of improving capability that is likely to provide benefit to reanalysis, especially for capturing extreme events like droughts and heat waves. Implementation of an improved land model that includes dynamic phenology and photosynthesis is a key component of the GMAO’s land surface modeling and

assimilation efforts (Koster et al. 2014). To improve the specification of ocean surface boundary conditions, many centers are developing some form of coupled ocean–atmosphere analysis system. The GMAO has recently implemented a coupled data assimilation scheme for analyzing ocean skin temperature within the existing atmospheric analysis (Akella et al. 2016). It uses background fields from a near-surface ocean diurnal layer model to assimilate surface-sensitive radiances plus in situ observations along with all other observations in the atmospheric assimilation system. The scheme may be described as being weakly coupled in the sense that the atmospheric observations do not affect the ocean fields directly, but only through the increment of ocean skin temperature during the next analysis cycle.

Improving the representation of aerosol effects on climate is another important area of development for reanalysis. As the aerosol observing system continues to evolve and provide additional global information on aerosol absorption, size, and vertical distribution, the discrepancy among reanalyses and satellite-only estimates of aerosol radiative-climate effects should decrease. For example, the GMAO is working to incorporate aerosol vertical distribution information from space-based lidars, as well as implicit speciation and size information from multichannel radiometers on low-orbiting and geostationary satellites. Unlike satellite estimates alone, reanalyses like MERRA-2 can provide detailed information on how the anthropogenic component of aerosols, and thus radiative forcing, has changed during the modern satellite era, as well as its interaction with the circulation and the climate at large. This should lead to reduced uncertainty in assessing, for example, the human impact on climate.

More extensive analysis coupling between the atmosphere, ocean, land, and chemistry as envisioned for IESA, while progressing, still presents significant challenges (e.g., Brassington et al. 2015). These include model biases that can be exacerbated when coupled, component systems with different physical characteristics and different spatial and temporal scales, and component observations in different media with different spatial and temporal frequencies and different latencies. These challenges may be offset at least partially by the fact that, in practice, where the time scales and observation latencies between components differ greatly—for example, as between the deep ocean and atmosphere—a weak coupling approach may suffice. Prospects for success are also bolstered by the fact that the numerical weather prediction community is placing increasing focus on the need to analyze currently uncoupled components of the Earth system in a more consistent manner. The GMAO

strategy is to progress incrementally toward an IESA through an evolving combination of coupled systems and offline component reanalyses driven by, for example, MERRA-2 atmospheric forcing.

Quantifying uncertainty in reanalyses remains important for expanding their utility, especially as a potential tool for climate change assessment. Dee et al. (2011) argued that advances in observational bias correction and other aspects of data assimilation have reduced uncertainty in the representation of low-frequency variability to the point where ERA-Interim can be used to estimate certain atmospheric temperature trends. More recently, Simmons et al. (2014) compared multiannual variability and trends in atmospheric temperature from ERA-Interim, JRA-55, and MERRA and found them to be in generally good agreement in the upper troposphere and lower stratosphere but more uncertain in the middle stratosphere. Nonetheless, for less well constrained quantities, such as precipitation and surface fluxes, there still appear to be substantial differences between recent reanalyses. For example, the 12-month running mean values of global precipitation in ERA-Interim, MERRA-2, and JRA-55 can at times differ by almost 20%. Uncertainty in sea surface temperature, as illustrated by the surprising differences between the prescribed values used in different reanalyses (Fig. 5) is likely to be a contributing factor. Impacts from observing system changes also appear to play a significant role in explaining these precipitation differences, pointing to the need for new sources of high-quality observations of these or closely related variables not only for assimilation but for improving our understanding and modeling of the underlying physical processes. Ongoing efforts to improve the quality of existing historical datasets are also critical in this regard.

The increasing use of ensemble and hybrid ensemble–variational methods in Earth system data assimilation has the potential to make at least some measures of uncertainty a standard component of reanalysis datasets (e.g., Compo et al. 2011; Poli et al. 2013). The GMAO has recently implemented a hybrid 4DENVAR scheme with similar capability. Finally, ECMWF, JMA, and GMAO are conducting multidecadal atmospheric model integrations (without data assimilation) for comparison with reanalyses as a means of assessing internal variability and distinguishing boundary-forced climate signals from those imposed by changes in the observing system. All these efforts will benefit from the continued assessment of existing reanalysis products by the research community and from the sharing of key data assimilation diagnostic quantities (e.g., background departures, analysis increments, and bias estimates) between both reanalysis developers and data providers.

Acknowledgments. Development of the GEOS data assimilation system and the MERRA-2 project were funded by NASA's Modeling, Analysis and Prediction program. Computational resources and support for the execution of MERRA-2 were provided by the NASA High-End Computing Capability Project and NASA Center for Climate Simulation. GEOS and MERRA-2 are the result of years of dedicated research, development, and analysis by many individuals at GMAO, whose efforts are greatly appreciated. We gratefully acknowledge the GMAO operations group for monitoring the production of MERRA-2 and the GMAO software integration group, who helped improve the performance and flexibility of GEOS. We thank Julio Bacmeister for his contribution to the development of the model physics, Qing Liu for processing the precipitation input data, and Allison Collow and Edmond Brent Smith for providing some of the figures for this paper. We also thank the GES DISC for providing online access to MERRA-2 products. Finally, we thank the three reviewers, whose comments and suggestions helped improve the paper substantially.

APPENDIX

Acronyms

3DVAR	Three-dimensional variational data assimilation	CFSR	Climate Forecast System Reanalysis
4DENVAR	Four-dimensional ensemble–variational data assimilation	CAMS	Copernicus Atmosphere Monitoring Service
AAOD	Aerosol absorption optical depth	CMIP	Coupled Model Intercomparison Project
ACARS	Aircraft Communications, Addressing, and Reporting System	CPC	Climate Prediction Center
AeroCom	Aerosol Comparison Project	CrIS	Cross-Track Infrared Sounder
AERONET	Aerosol Robotics Network	CRTM	Community Radiative Transfer Model
AIREP	Aircraft report	DRE	Direct radiative effect
AIRS	Advanced Infrared Sounder	ECMWF	European Centre for Medium-Range Weather Forecasts
AMDAR	Aircraft Meteorological Data Relay	EOS	Earth Observing System
AMSR-E	Advanced Microwave Scanning Radiometer for EOS	ERA-20C	ECMWF twentieth century reanalysis (from 1900 to 2010)
AMSU-A	Advanced Microwave Sounding Unit A	ERA-Interim	ECMWF interim reanalysis (from 1979 to present)
AMSU-B	Advanced Microwave Sounding Unit B	ERS	European Remote-Sensing Satellites
AOD	Aerosol optical depth	FGAT	First guess at appropriate time
ASCAT	Advanced Scatterometer	GEOS	Goddard Earth Observing System
ASDAR	Aircraft to Satellite Data Relay	GES DISC	Goddard Earth Sciences Data Information Services Center
ATMS	Advanced Technology Microwave Sounder	GLATOVS	Goddard Laboratory for Atmospheres TOVS forward model
ATOVS	Advanced TIROS Operational Vertical Sounder	GMAO	Global Modeling and Assimilation Office
AVHRR	Advanced Very High Resolution Radiometer	GMS	Geostationary Meteorological Satellite
BoM	Bureau of Meteorology (Australia)	GOCART	Goddard Chemistry Aerosol Radiation and Transport
		GOES	Geostationary Operational Environmental Satellites
		GPCP	Global Precipitation Climatology Project
		GPSRO	Global positioning system radio occultation
		GSI	Gridpoint Statistical Interpolation
		GWD	Gravity wave drag
		HIRS	High Resolution Infrared Radiation Sounder
		IASI	Infrared Atmospheric Sounding Interferometer
		IAU	Incremental analysis update
		IESA	Integrated Earth system analysis
		IPCC	Intergovernmental Panel on Climate Change
		JMA	Japan Meteorological Agency
		JPSS	Joint Polar Satellite System
		JRA-55	Japanese 55-year Reanalysis
		MACC	Monitoring Atmospheric Composition and Climate project
		MAR	Modèle Atmosphérique Régional
		MDCRS	Meteorological Data Collection and Reporting System
		MERRA	Modern-Era Retrospective Analysis for Research and Applications
		MERRA-2	Modern-Era Retrospective Analysis for Research and Applications, version 2

MetOp	Meteorological Operational Satellites
MHS	Microwave Humidity Sounder
MISR	Multiangle Imaging Spectro Radiometer
MLS	Microwave Limb Sounder
MODIS	Moderate Resolution Imaging Spectroradiometer
MSG	Meteosat Second Generation
MSU	Microwave Sounding Unit
MTSAT	Multifunctional Transport Satellite
NAAPS	Navy Aerosol Analysis and Prediction System
NASA	National Aeronautics and Space Administration
NCEP	National Centers for Environmental Prediction
NEXRAD	Next Generation Weather Radar
NMC	National Meteorological Center
NOAA	National Oceanic and Atmospheric Administration
NRL	Naval Research Laboratory
OISST	Optimum Interpolation Sea Surface Temperature
OMI	Ozone Monitoring Instrument
OPAC	Optical Properties of Aerosols and Clouds
OSTIA	Operational Sea Surface Temperature and Sea Ice Analysis
PAOB	Synthetic surface pressure observation
Pibal	Pilot balloon
PIREP	Pilot report
QBO	Quasi-biennial oscillation
Raob	Radiosonde observation
RAS	Relaxed Arakawa–Schubert convection scheme
RMS	Root-mean-square
RSS	Remote Sensing Systems
SBUV	Solar Backscatter Ultraviolet Radiometer
SEVIRI	Spinning Enhanced Visible Infrared Imager
SHEBA	Surface Heat Budget of the Arctic Ocean
SIC	Sea ice concentration
SMAP	Soil Moisture Active Passive satellite
SMOS	Soil Moisture and Ocean Salinity satellite
SNPP	<i>Suomi National Polar-Orbiting Partnership</i>
SSM/I	Special Sensor Microwave Imager
SSMIS	Special Sensor Microwave Imager/Sounder
SST	Sea surface temperature
SSU	Stratospheric Sounding Unit
TIROS	Television Infrared Observation Satellite
TMI	Tropical Rainfall Measuring Mission Microwave Imager
TOA	Top of the atmosphere

TOMS	Total Ozone Mapping Spectrometer
VAD	Velocity Azimuth Display
WMO	World Meteorological Organization

REFERENCES

- Adler, R. F., and Coauthors, 2003: The Version-2 Global Precipitation Climatology Project (GPCP) monthly precipitation analysis (1979–present). *J. Hydrometeor.*, **4**, 1147–1167, doi:[10.1175/1525-7541\(2003\)004<1147:TGPCP>2.0.CO;2](https://doi.org/10.1175/1525-7541(2003)004<1147:TGPCP>2.0.CO;2).
- Akella, S., R. Todling, and M. Suárez, 2016: Assimilation for skin SST in the NASA GEOS atmospheric data assimilation system. *Quart. J. Roy. Meteor. Soc.*, **143**, 1032–1046, doi:[10.1002/qj.2988](https://doi.org/10.1002/qj.2988).
- Andrews, D. G., J. R. Holton, and C. B. Leovy, 1987: *Middle Atmosphere Dynamics*. Academic Press, 489 pages.
- Bacmeister, J. T., and G. Stephens, 2011: Spatial statistics of likely convective clouds in CloudSat data. *J. Geophys. Res.*, **116**, D04104, doi:[10.1029/2010JD014444](https://doi.org/10.1029/2010JD014444).
- Ballish, B. A., and V. K. Kumar, 2008: Systematic differences in aircraft and radiosonde temperatures. *Bull. Amer. Meteor. Soc.*, **89**, 1689–1707, doi:[10.1175/2008BAMS2332.1](https://doi.org/10.1175/2008BAMS2332.1).
- Bauer, P., A. J. Geer, P. Lopez, and D. Salmon, 2010: Direct 4D-Var assimilation of all-sky radiances. Part I: Implementation. *Quart. J. Roy. Meteor. Soc.*, **136**, 1868–1885, doi:[10.1002/qj.659](https://doi.org/10.1002/qj.659).
- Bellouin, N., J. Quaas, J.-J. Morcrette, and O. Boucher, 2013: Estimates of aerosol radiative forcing from the MACC reanalysis. *Atmos. Chem. Phys.*, **13**, 2045–2062, doi:[10.5194/acp-13-2045-2013](https://doi.org/10.5194/acp-13-2045-2013).
- Berrisford, P., P. Kallberg, S. Kobayashi, D. Dee, S. Uppala, A. J. Simmons, P. Poli, and H. Sato, 2011: Atmospheric conservation properties in ERA-Interim. *Quart. J. Roy. Meteor. Soc.*, **137**, 1381–1399, doi:[10.1002/qj.864](https://doi.org/10.1002/qj.864).
- Bloom, S., L. Takacs, A. DaSilva, and D. Ledvina, 1996: Data assimilation using incremental analysis updates. *Mon. Wea. Rev.*, **124**, 1256–1271, doi:[10.1175/1520-0493\(1996\)124<1256:DAUIAU>2.0.CO;2](https://doi.org/10.1175/1520-0493(1996)124<1256:DAUIAU>2.0.CO;2).
- Bocquet, M., and Coauthors, 2015: Data assimilation in atmospheric chemistry models: Current and future prospects for coupled chemistry meteorology models. *Atmos. Chem. Phys.*, **15**, 5325–5358, doi:[10.5194/acp-15-5325-2015](https://doi.org/10.5194/acp-15-5325-2015).
- Bosilovich, M. G., 2013: Regional climate and variability in NASA MERRA and recent reanalyses: U.S. summertime precipitation and temperature. *J. Appl. Meteor. Climatol.*, **52**, 1939–1951, doi:[10.1175/JAMC-D-12-0291.1](https://doi.org/10.1175/JAMC-D-12-0291.1).
- , F. R. Robertson, and J. Chen, 2011: Global energy and water budgets in MERRA. *J. Climate*, **24**, 5721–5739, doi:[10.1175/2011JCLI4175.1](https://doi.org/10.1175/2011JCLI4175.1).
- , and Coauthors, 2015: MERRA-2: Initial evaluation of the climate. Technical Report Series on Global Modeling and Data Assimilation, Vol. 43, NASA Tech. Rep. NASA/TM-2015-104606, 139 pp. [Available online at <https://gmao.gsfc.nasa.gov/pubs/docs/Bosilovich803.pdf>.]
- , R. Lucchesi, and M. Suarez, 2016: MERRA-2: File specification. GMAO Office Note 9, 73 pp. [Available online at <https://gmao.gsfc.nasa.gov/pubs/docs/Bosilovich785.pdf>.]
- , F. Robertson, L. Takacs, A. Molod, and D. Mocko, 2017: Atmospheric water balance and variability in the MERRA-2 reanalysis. *J. Climate*, **30**, 1177–1196, doi:[10.1175/JCLI-D-16-0338.1](https://doi.org/10.1175/JCLI-D-16-0338.1).
- Box, J. E., and A. Rinke, 2003: Evaluation of Greenland Ice Sheet surface climate in the HIRHAM regional climate model using

- automatic weather station data. *J. Climate*, **16**, 1302–1319, doi:[10.1175/1520-0442-16.9.1302](https://doi.org/10.1175/1520-0442-16.9.1302).
- Brassington, G. B., and Coauthors, 2015: Progress and challenges in short- to medium- range coupled prediction. *J. Oper. Oceanogr.*, **8**, 239–258, doi:[10.1080/1755876X.2015.1049875](https://doi.org/10.1080/1755876X.2015.1049875).
- Buchard, V., and Coauthors, 2015: Using the OMI aerosol index and absorption aerosol optical depth to evaluate the NASA MERRA Aerosol Reanalysis. *Atmos. Chem. Phys.*, **15**, 5743–5760, doi:[10.5194/acp-15-5743-2015](https://doi.org/10.5194/acp-15-5743-2015).
- Cardinali, C., L. Isaksen, and E. Anderson, 2003: Use and impact of automated aircraft data in a global 4DVAR data assimilation system. *Mon. Wea. Rev.*, **131**, 1865–1877, doi:[10.1175/2569.1](https://doi.org/10.1175/2569.1).
- Chen, Y., F. Weng, Y. Han, and Q. Liu, 2008: Validation of the Community Radiative Transfer Model (CRTM) by using CloudSat data. *J. Geophys. Res.*, **113**, 2156–2202, doi:[10.1029/2007JD009561](https://doi.org/10.1029/2007JD009561).
- Chin, M., and Coauthors, 2002: Tropospheric aerosol optical thickness from the GOCART model and comparisons with satellite and sun photometer measurements. *J. Atmos. Sci.*, **59**, 461–483, doi:[10.1175/1520-0469\(2002\)059<0461:TAOTFT>2.0.CO;2](https://doi.org/10.1175/1520-0469(2002)059<0461:TAOTFT>2.0.CO;2).
- Chýlek, P., and J. A. Coakley, 1974: Aerosol and climate. *Science*, **183**, 75–77, doi:[10.1126/science.183.4120.75](https://doi.org/10.1126/science.183.4120.75).
- Colarco, P., A. da Silva, M. Chin, and T. Diehl, 2010: Online simulations of global aerosol distributions in the NASA GEOS-4 model and comparisons to satellite and ground-based aerosol optical depth. *J. Geophys. Res.*, **115**, D14207, doi:[10.1029/2009JD012820](https://doi.org/10.1029/2009JD012820).
- Collow, A. B. M., and M. A. Miller, 2016: The seasonal cycle of the radiation budget and cloud radiative effect in the Amazon rain forest of Brazil. *J. Climate*, **29**, 7703–7722, doi:[10.1175/JCLI-D-16-0089.1](https://doi.org/10.1175/JCLI-D-16-0089.1).
- , M. G. Bosilovich, and R. D. Koster, 2016: Large-scale influences on summertime extreme precipitation in the north-eastern United States. *J. Hydrometeor.*, **17**, 3045–3061, doi:[10.1175/JHM-D-16-0091.1](https://doi.org/10.1175/JHM-D-16-0091.1).
- Colony, R., I. Appel, and I. Rigor, 1992: Surface air temperature observations in the Arctic Basin. Applied Physics Laboratory, University of Washington Tech. Memo. TM 1-92, 120 pp.
- Compo, G. P., and Coauthors, 2011: The Twentieth Century Reanalysis Project. *Quart. J. Roy. Meteor. Soc.*, **137**, 1–28, doi:[10.1002/qj.776](https://doi.org/10.1002/qj.776).
- Coy, L., K. Wargin, A. M. Molod, W. R. McCarty, and S. Pawson, 2016: Structure and dynamics of the quasi-biennial oscillation in MERRA-2. *J. Climate*, **29**, 5339–5354, doi:[10.1175/JCLI-D-15-0809.1](https://doi.org/10.1175/JCLI-D-15-0809.1).
- Cullather, R. I., and M. G. Bosilovich, 2012: The energy budget of the polar atmosphere in MERRA. *J. Climate*, **25**, 5–24, doi:[10.1175/2011JCLI4138.1](https://doi.org/10.1175/2011JCLI4138.1).
- , S. M. J. Nowicki, B. Zhao, and M. J. Suárez, 2014: Evaluation of the surface representation of the Greenland Ice Sheet in a general circulation model. *J. Climate*, **27**, 4835–4856, doi:[10.1175/JCLI-D-13-00635.1](https://doi.org/10.1175/JCLI-D-13-00635.1).
- Darmenov, A., and A. da Silva, 2015: The Quick Fire Emissions Dataset (QFED): Documentation of versions 2.1, 2.2 and 2.4. Technical Report Series on Global Modeling and Data Assimilation, Vol. 32, NASA Tech. Rep. NASA/TM-2015-104606, 201 pp. [Available online at <https://gmao.gsfc.nasa.gov/pubs/docs/Darmenov796.pdf>.]
- Decker, M., M. A. Brunke, Z. Wang, K. Sakaguchi, X. Zeng, and M. G. Bosilovich, 2011: Evaluation of the reanalysis products from GSFC, NCEP, and ECMWF using flux tower observations. *J. Climate*, **24**, 221–249, doi:[10.1175/JCLI-D-11-00004.1](https://doi.org/10.1175/JCLI-D-11-00004.1).
- Dee, D. P., and A. M. da Silva, 2003: The choice of variable for atmospheric moisture analysis. *Mon. Wea. Rev.*, **131**, 155–171, doi:[10.1175/1520-0493\(2003\)131<0155:TCOVFA>2.0.CO;2](https://doi.org/10.1175/1520-0493(2003)131<0155:TCOVFA>2.0.CO;2).
- , and S. Uppala, 2009: Variational bias correction of satellite radiance data in the ERA-Interim reanalysis. *Quart. J. Roy. Meteor. Soc.*, **135**, 1830–1841, doi:[10.1002/qj.493](https://doi.org/10.1002/qj.493).
- , and Coauthors, 2011: The ERA-Interim reanalysis: Configuration and performance of the data assimilation system. *Quart. J. Roy. Meteor. Soc.*, **137**, 553–597, doi:[10.1002/qj.828](https://doi.org/10.1002/qj.828).
- Derber, J. C., and W.-S. Wu, 1998: The use of TOVS cloud-cleared radiances in the NCEP SSI analysis system. *Mon. Wea. Rev.*, **126**, 2287–2299, doi:[10.1175/1520-0493\(1998\)126<2287:TUOTCC>2.0.CO;2](https://doi.org/10.1175/1520-0493(1998)126<2287:TUOTCC>2.0.CO;2).
- Diehl, T., A. Heil, M. Chin, X. Pan, D. Streets, M. Schultz, and S. Kinne, 2012: Anthropogenic, biomass burning, and volcanic emissions of black carbon, organic carbon, and SO₂ from 1980 to 2010 for hindcast model experiments. *Atmos. Chem. Phys. Discuss.*, **12**, 24 895–24 954, doi:[10.5194/acpd-12-24895-2012](https://doi.org/10.5194/acpd-12-24895-2012).
- Donlon, C. J., M. Martin, J. Stark, J. Roberts-Jones, E. Fiedler, and W. Wimmer, 2012: The Operational Sea Surface Temperature and Sea Ice Analysis (OSTIA) system. *Remote Sens. Environ.*, **116**, 140–158, doi:[10.1016/j.rse.2010.10.017](https://doi.org/10.1016/j.rse.2010.10.017).
- Duyunkerke, P., and S. de Roode, 2001: Surface energy balance and turbulence characteristics observed at the SHEBA Ice Camp during FIRE III. *J. Geophys. Res.*, **106**, 15 313–15 322, doi:[10.1029/2000JD900537](https://doi.org/10.1029/2000JD900537).
- Farman, J., B. Gardiner, and J. Shanklin, 1985: Large losses of total ozone in Antarctica reveal seasonal ClO_x/NO_x interaction. *Nature*, **315**, 207–210, doi:[10.1038/315207a0](https://doi.org/10.1038/315207a0).
- Fettweis, X., 2007: Reconstruction of the 1979–2006 Greenland ice sheet surface mass balance using the regional climate model MAR. *Cryosphere*, **1**, 21–40, doi:[10.5194/tc-1-21-2007](https://doi.org/10.5194/tc-1-21-2007).
- Flemming, J., and Coauthors, 2017: The CAMS interim reanalysis of carbon monoxide, ozone and aerosol for 2003–2015. *Atmos. Chem. Phys.*, **17**, 1945–1983, doi:[10.5194/acp-17-1945-2017](https://doi.org/10.5194/acp-17-1945-2017).
- Froidevaux, L., and Coauthors, 2006: Early validation analyses of atmospheric profiles from EOS MLS on the Aura satellite. *IEEE Trans. Geosci. Remote Sens.*, **44**, 1106–1121, doi:[10.1109/TGRS.2006.864366](https://doi.org/10.1109/TGRS.2006.864366).
- GMAO, 2015a: MERRA-2 inst1_2d_asm_Nx: 2d, 3-hourly, instantaneous, single-level, assimilation, single-level diagnostics V5.12.4. GES DISC, accessed June 2016, doi:[10.5067/3Z173KIE2TPD](https://doi.org/10.5067/3Z173KIE2TPD).
- , 2015b: MERRA-2 inst1_2d_int_Nx: 2d, 1-hourly, instantaneous, single-level, assimilation, vertically integrated diagnostics V5.12.4. GES DISC, accessed June 2016, doi:[10.5067/G0U6NGQ3BLE0](https://doi.org/10.5067/G0U6NGQ3BLE0).
- , 2015c: MERRA-2 inst3_3d_asm_Np: 3d, 3-hourly, instantaneous, pressure-level, assimilation, assimilated meteorological fields, V5.12.4. Goddard Space Flight Center Distributed Active Archive Center, accessed June 2016, doi:[10.5067/QBZ6MG944HW0](https://doi.org/10.5067/QBZ6MG944HW0).
- , 2015d: MERRA-2 tavg1_2d_flx_Nx: 2d, 1-hourly, time-averaged, single-level, assimilation, surface flux diagnostics V5.12.4. GES DISC, accessed June 2016, doi:[10.5067/7MCPBJ41YOK6](https://doi.org/10.5067/7MCPBJ41YOK6).
- , 2015e: MERRA-2 tavg1_2d_int_Nx: 2d, 1-hourly, time-averaged, single-level, assimilation, vertically integrated diagnostics V5.12.4. GES DISC, accessed June 2016, doi:[10.5067/Q5GVUVUIVGO7](https://doi.org/10.5067/Q5GVUVUIVGO7).
- , 2015f: MERRA-2 tavg1_2d_slv_Nx: 2d, 1-hourly, time-averaged, single-level, assimilation, single-level diagnostics V5.12.4. GES DISC, accessed June 2016, doi:[10.5067/VJAFPLI1CSIV](https://doi.org/10.5067/VJAFPLI1CSIV).
- , 2015g: MERRA-2 tavgM_2d_aer_Nx: 2d, monthly mean, time-averaged, single-level, assimilation, aerosol diagnostics

- V5.12.4. Goddard Space Flight Center Distributed Active Archive Center, accessed June 2016, doi:[10.5067/FH9A0MLJPC7N](https://doi.org/10.5067/FH9A0MLJPC7N).
- , 2015h: MERRA-2 tavgM_2d_fx_Nx: 2d, monthly mean, time-averaged, single-level, assimilation, surface flux diagnostics V5.12.4. GES DISC, accessed June 2016, doi:[10.5067/0JRLVL8YV2Y4](https://doi.org/10.5067/0JRLVL8YV2Y4).
- , 2015i: MERRA-2 tavgM_2d_glc_Nx: 2d, monthly mean, land ice surface diagnostics, V5.12.4. Goddard Space Flight Center Distributed Active Archive Center, accessed June 2015, doi:[10.5067/5WQ319WUFGX](https://doi.org/10.5067/5WQ319WUFGX).
- , 2015j: MERRA-2 tavgM_2d_lnd_Nx: 2d, monthly mean, land surface diagnostics, V5.12.4. Goddard Space Flight Center Distributed Active Archive Center, accessed June 2015, doi:[10.5067/8S35XF81C28F](https://doi.org/10.5067/8S35XF81C28F).
- , 2015k: MERRA-2 tavgM_2d_int_Nx: 2d, monthly mean, time-averaged, single-level, assimilation, vertically integrated diagnostics V5.12.4. GES DISC, accessed June 2015, doi:[10.5067/FQPTQ4OJ22TL](https://doi.org/10.5067/FQPTQ4OJ22TL).
- , 2015l: MERRA-2 tavgM_3d_qdt_Np: 3d, monthly mean, time-averaged, pressure-level, assimilation, moist tendencies V5.12.4. GES DISC, accessed June 2016, doi:[10.5067/2ZTU87V69ATP](https://doi.org/10.5067/2ZTU87V69ATP).
- , 2015m: MERRA-2 tavgM_2d_slv_Nx: 2d, monthly mean, single-level diagnostics, V5.12.4. Goddard Space Flight Center Distributed Active Archive Center, accessed April 2015, doi:[10.5067/AP1B0BA5PD2K](https://doi.org/10.5067/AP1B0BA5PD2K).
- , 2015n: MERRA-2 tavgM_3d_tdt_Np: 3d, monthly mean, time-averaged, pressure-level, assimilation, temperature tendencies V5.12.4. GES DISC, accessed June 2016, doi:[10.5067/VILT59HI2MOY](https://doi.org/10.5067/VILT59HI2MOY).
- Gong, S. L., 2003: A parameterization of sea-salt aerosol source function for sub- and super-micron particles. *Global Biogeochem. Cycles*, **17**, 1097, doi:[10.1029/2003GB002079](https://doi.org/10.1029/2003GB002079).
- Greuell, W., and T. Konzelmann, 1994: Numerical modelling of the energy balance and englacial temperature of the Greenland Ice Sheet. Calculations for the ETH-Camp location (West Greenland, 1155 m a.s.l.). *Global Planet. Change*, **9**, 91–114, doi:[10.1016/0921-8181\(94\)90010-8](https://doi.org/10.1016/0921-8181(94)90010-8).
- Ham, Y.-G., S. Schubert, Y. Vikhlaev, and M. J. Suárez, 2014: An assessment of the ENSO forecast skill of GEOS-5 system. *Climate Dyn.*, **43**, 2415, doi: [10.1007/s00382-014-2063-2](https://doi.org/10.1007/s00382-014-2063-2).
- Han, Y., P. van Delst, Q. Liu, F. Weng, B. Yan, R. Treadon, and J. Derber, 2006: JCSDA Community Radiative Transfer Model (CRTM)—Version 1. NOAA Tech. Rep. 122, 33 pp. [Available online at https://docs.lib.noaa.gov/noaa_documents/NESDIS/TR_NESDIS/TR_NESDIS_122.pdf.]
- Heidinger, A. K., C. Cao, and J. T. Sullivan, 2002: Using Moderate Resolution Imaging Spectrometer (MODIS) to calibrate Advanced Very High Resolution Radiometer reflectance channels. *J. Geophys. Res.*, **107**, 4702, doi:[10.1029/2001JD002035](https://doi.org/10.1029/2001JD002035).
- Hoch, S. W., 2005: Radiative flux divergence in the surface boundary layer. A study based on observations at Summit, Greenland. Ph.D. dissertation, Swiss Federal Institute of Technology, 164 pp.
- Holben, B., and Coauthors, 1998: AERONET—A federated instrument network and data archive for aerosol characterization. *Remote Sens. Environ.*, **66**, 1–16, doi:[10.1016/S0034-4257\(98\)00031-5](https://doi.org/10.1016/S0034-4257(98)00031-5).
- Holm, E. V., 2003: Revision of the ECMWF humidity analysis: Construction of a Gaussian control variable. *Proc. ECMWF/GEWEX Workshop on Humidity Analysis*, Reading, United Kingdom, ECMWF/GEWEX, 6 pp. [Available online at <http://www.ecmwf.int/sites/default/files/elibrary/2003/9998-revision-ecmwf-humidity-analysis-construction-gaussian-control-variable.pdf>.]
- Inness, A. F., and Coauthors, 2013: The MACC reanalysis: An 8 yr data set of atmospheric composition. *Atmos. Chem. Phys.*, **13**, 4073–4109, doi:[10.5194/acp-13-4073-2013](https://doi.org/10.5194/acp-13-4073-2013).
- Kahn, R. A., B. J. Gaitley, J. V. Martonchik, D. J. Diner, K. A. Crean, and B. Holben, 2005: Multiangle Imaging Spectroradiometer (MISR) global aerosol optical depth validation based on 2 years of coincident Aerosol Robotic Network (AERONET) observations. *J. Geophys. Res.*, **110**, D10S04, doi:[10.1029/2004JD004706](https://doi.org/10.1029/2004JD004706).
- Kinne, S., and Coauthors, 2006: An AeroCom initial assessment—Optical properties in aerosol component modules of global models. *Atmos. Chem. Phys.*, **6**, 1815–1834, doi:[10.5194/acp-6-1815-2006](https://doi.org/10.5194/acp-6-1815-2006).
- Kleist, D. T., D. F. Parrish, J. C. Derber, R. Treadon, R. M. Errico, and R. Yang, 2009a: Improving incremental balance in the GSI 3DVAR analysis system. *Mon. Wea. Rev.*, **137**, 1046–1060, doi:[10.1175/2008MWR2623.1](https://doi.org/10.1175/2008MWR2623.1).
- , —, —, —, W.-S. Wu, and S. Lord, 2009b: Introduction of the GSI into the NCEPs Global Data Assimilation System. *Wea. Forecasting*, **24**, 1691–1705, doi:[10.1175/2009WA222201.1](https://doi.org/10.1175/2009WA222201.1).
- Kobayashi, S., M. Matricardi, D. Dee, and S. Uppala, 2009: Toward a consistent reanalysis of the upper stratosphere based on radiance measurements from SSU and AMSU-A. *Quart. J. Roy. Meteor. Soc.*, **135**, 2086–2099, doi:[10.1002/qj.514](https://doi.org/10.1002/qj.514).
- , and Coauthors, 2015: The JRA-55 reanalysis: General specifications and basic characteristics. *J. Meteor. Soc. Japan*, **93**, 5–48, doi:[10.2151/jmsj.2015-001](https://doi.org/10.2151/jmsj.2015-001).
- Koster, R. D., G. Walker, G. J. Collatz, and P. E. Thornton, 2014: Hydroclimatic controls on the means and variability of vegetation phenology and carbon uptake. *J. Climate*, **27**, 5632–5652, doi:[10.1175/JCLI-D-13-00477.1](https://doi.org/10.1175/JCLI-D-13-00477.1).
- Kunkel, K. E., and Coauthors, 2013: Monitoring and understanding trends in extreme storms: State of knowledge. *Bull. Amer. Meteor. Soc.*, **94**, 499–514, doi:[10.1175/BAMS-D-11-00262.1](https://doi.org/10.1175/BAMS-D-11-00262.1).
- Levy, R. C., L. A. Remer, S. Mattoo, E. F. Vermote, and Y. J. Kaufman, 2007: Second-generation operational algorithm: Retrieval of aerosol properties over land from inversion of Moderate Resolution Imaging Spectroradiometer spectral reflectance. *J. Geophys. Res.*, **112**, D13211, doi:[10.1029/2006JD007811](https://doi.org/10.1029/2006JD007811).
- Lim, Y.-K., R. Kovach, S. Pawson, and G. Vernieres, 2017: The 2015/16 El Niño event in context of the MERRA-2 reanalysis: A comparison of the tropical Pacific with 1982/83 and 1997/98. *J. Climate*, doi:[10.1175/JCLI-D-16-0800.1](https://doi.org/10.1175/JCLI-D-16-0800.1), in press.
- Liu, Q., and S. Boukabara, 2014: Community Radiative Transfer Model (CRTM) applications in supporting the Suomi National Polar-Orbiting Partnership (SNPP) mission validation and verification. *Remote Sens. Environ.*, **140**, 744–754, doi:[10.1016/j.rse.2013.10.011](https://doi.org/10.1016/j.rse.2013.10.011).
- Lynch, P., and Coauthors, 2016: An 11-year global gridded aerosol optical thickness reanalysis (v1.0) for atmospheric and climate sciences. *Geosci. Model Dev.*, **9**, 1489–1522, doi:[10.5194/gmd-9-1489-2016](https://doi.org/10.5194/gmd-9-1489-2016).
- Lynch-Stieglitz, M., 1994: The development and validation of a simple snow model for the GISS GCM. *J. Climate*, **7**, 1842–1855, doi:[10.1175/1520-0442\(1994\)007<1842:TDAVOA>2.0.CO;2](https://doi.org/10.1175/1520-0442(1994)007<1842:TDAVOA>2.0.CO;2).
- Manney, G. L., and Coauthors, 2008: The evolution of the stratosphere during the 2006 major warming: Satellite data and

- assimilated meteorological analyses. *J. Geophys. Res.*, **113**, D11115, doi:[10.1029/2007JD009097](https://doi.org/10.1029/2007JD009097).
- Marticorena, B., and G. Bergametti, 1995: Modeling the atmospheric dust cycle: 1. Design of a soil-derived dust emission scheme. *J. Geophys. Res.*, **100**, 16 415–16 430, doi:[10.1029/95JD00690](https://doi.org/10.1029/95JD00690).
- McCarty, W., L. Coy, R. Gelaro, A. Huang, D. Merkova, E. B. Smith, M. Sienkiewicz, and K. Wargan, 2016: MERRA-2 input observations: Summary and initial assessment. Technical Report Series on Global Modeling and Data Assimilation, Vol. 46, NASA Tech. Rep. NASA/TM-2016-104606, 61 pp. [Available online at <https://gmao.gsfc.nasa.gov/pubs/docs/McCarty885.pdf>.]
- McPeters, R., and Coauthors, 2008: Validation of the Aura Ozone Monitoring Instrument total column ozone product. *J. Geophys. Res.*, **113**, D15S14, doi:[10.1029/2007JD008802](https://doi.org/10.1029/2007JD008802).
- Meng, J., R. Yang, H. Wei, M. Ek, G. Gayno, P. Xie, and K. Mitchell, 2012: The Land Surface Analysis in the NCEP Climate Forecast System Reanalysis. *J. Hydrometeorol.*, **13**, 1621–1630, doi:[10.1175/JHM-D-11-090.1](https://doi.org/10.1175/JHM-D-11-090.1).
- Mesinger, F., and Coauthors, 2006: North American Regional Reanalysis. *Bull. Amer. Meteor. Soc.*, **87**, 343–360, doi:[10.1175/BAMS-87-3-343](https://doi.org/10.1175/BAMS-87-3-343).
- Molina, M. J., and F. S. Rowland, 1974: Stratospheric sink for chlorofluoromethanes: Chlorine atom-catalysed destruction of ozone. *Nature*, **249**, 810–812, doi:[10.1038/249810a0](https://doi.org/10.1038/249810a0).
- Molod, A., L. Takacs, M. Suárez, and J. Bacmeister, 2015: Development of the GEOS-5 atmospheric general circulation model: Evolution from MERRA to MERRA2. *Geosci. Model Dev.*, **8**, 1339–1356, doi:[10.5194/gmd-8-1339-2015](https://doi.org/10.5194/gmd-8-1339-2015).
- Moorthi, S., and M. J. Suárez, 1992: Relaxed Arakawa–Schubert: A parameterization of moist convection for general circulation models. *Mon. Wea. Rev.*, **120**, 978–1002, doi:[10.1175/1520-0493\(1992\)120<0978:RASAPO>2.0.CO;2](https://doi.org/10.1175/1520-0493(1992)120<0978:RASAPO>2.0.CO;2).
- Myhre, G., 2009: Consistency between satellite-derived and modeled estimates of the direct aerosol effect. *Science*, **325**, 187–190, doi:[10.1126/science.1174461](https://doi.org/10.1126/science.1174461).
- Newman, P. A., and E. R. Nash, 2005: The unusual Southern Hemisphere stratosphere winter of 2002. *J. Atmos. Sci.*, **62**, 614–628, doi:[10.1175/JAS-3323.1](https://doi.org/10.1175/JAS-3323.1).
- Parrish, D. F., and J. C. Derber, 1992: The National Meteorological Center's spectral statistical-interpolation analysis system. *Mon. Wea. Rev.*, **120**, 1747–1763, doi:[10.1175/1520-0493\(1992\)120<1747:TNCMSS>2.0.CO;2](https://doi.org/10.1175/1520-0493(1992)120<1747:TNCMSS>2.0.CO;2).
- Poli, P., and Coauthors, 2013: The data assimilation system and initial performance evaluation of the ECMWF pilot reanalysis of the 20th-century assimilating surface observations only (ERA-20C). ERA Tech. Rep. 14, 59 pp. [Available online at <http://www.ecmwf.int/en/elibrary/11699-data-assimilation-system-and-initial-performance-evaluation-ecmwf-pilot-reanalysis>.]
- Putman, W., and S.-J. Lin, 2007: Finite-volume transport on various cubed-sphere grids. *J. Comput. Phys.*, **227**, 55–78, doi:[10.1016/j.jcp.2007.07.022](https://doi.org/10.1016/j.jcp.2007.07.022).
- Randles, C. A., and Coauthors, 2016: The MERRA-2 aerosol assimilation. Technical Report Series on Global Modeling and Data Assimilation, Vol. 45, NASA Tech. Rep. NASA/TM-2016-104606, 143 pp. [Available online at <https://gmao.gsfc.nasa.gov/pubs/docs/Randles887.pdf>.]
- , and Coauthors, 2017: The MERRA-2 aerosol reanalysis, 1980 onward. Part I: System description and data assimilation evaluation. *J. Climate*, doi:[10.1175/JCLI-D-16-0609.1](https://doi.org/10.1175/JCLI-D-16-0609.1), in press.
- Reichle, R. H., and Q. Liu, 2014: Observation-corrected precipitation estimates in GEOS-5. Technical Report Series on Global Modelling and Data Assimilation, Vol. 35, NASA Tech. Rep. NASA/TM-2014-104606, 24 pp. [Available online at <https://ntrs.nasa.gov/archive/nasa/casi.ntrs.nasa.gov/20150000725.pdf>.]
- , R. D. Koster, G. J. M. De Lannoy, B. A. Forman, Q. Liu, S. Mahanama, and A. Toure, 2011: Assessment and enhancement of MERRA land surface hydrology estimates. *J. Climate*, **24**, 6322–6338, doi:[10.1175/JCLI-D-10-05033.1](https://doi.org/10.1175/JCLI-D-10-05033.1).
- , Q. Liu, R. D. Koster, C. S. Draper, S. P. P. Mahanama, and G. S. Partyka, 2017a: Land surface precipitation in MERRA-2. *J. Climate*, **30**, 1643–1664, doi:[10.1175/JCLI-D-16-0570.1](https://doi.org/10.1175/JCLI-D-16-0570.1).
- , C. S. Draper, Q. Liu, M. Girotto, S. P. P. Mahanama, R. D. Koster, and G. J. M. De Lannoy, 2017b: Assessment of MERRA-2 land surface hydrology estimates. *J. Climate*, **30**, 2937–2960, doi:[10.1175/JCLI-D-16-0720.1](https://doi.org/10.1175/JCLI-D-16-0720.1).
- Remer, L. A., and Coauthors, 2005: The MODIS aerosol algorithm, products, and validation. *J. Atmos. Sci.*, **62**, 947–973, doi:[10.1175/JAS3385.1](https://doi.org/10.1175/JAS3385.1).
- Reynolds, R. W., N. A. Rayner, T. M. Smith, D. C. Stokes, and W. Wang, 2002: An improved in situ and satellite SST analysis for climate. *J. Climate*, **15**, 1609–1625, doi:[10.1175/1520-0442\(2002\)015<1609:AIISAS>2.0.CO;2](https://doi.org/10.1175/1520-0442(2002)015<1609:AIISAS>2.0.CO;2).
- , T. M. Smith, C. Liu, D. B. Chelton, K. S. Casey, and M. G. Schlax, 2007: Daily high-resolution-blended analyses for sea surface temperature. *J. Climate*, **20**, 5473–5496, doi:[10.1175/2007JCLI1824.1](https://doi.org/10.1175/2007JCLI1824.1).
- Rienecker, M. M., and Coauthors, 2008: The GEOS-5 Data Assimilation System—Documentation of versions 5.0.1, 5.1.0, and 5.2.0. Technical Report Series on Global Modeling and Data Assimilation, Vol. 27, NASA Tech. Rep. NASA/TM-2008-104606, 118 pp. [Available online at <https://gmao.gsfc.nasa.gov/pubs/docs/Rienecker369.pdf>.]
- , and Coauthors, 2011: MERRA: NASA's Modern-Era Retrospective Analysis for Research and Applications. *J. Climate*, **24**, 3624–3648, doi:[10.1175/JCLI-D-11-00015.1](https://doi.org/10.1175/JCLI-D-11-00015.1).
- Robertson, F. R., M. G. Bosilovich, J. Chen, and T. L. Miller, 2011: The effect of satellite observing system changes on MERRA water and energy fluxes. *J. Climate*, **24**, 5197–5217, doi:[10.1175/2011JCLI4227.1](https://doi.org/10.1175/2011JCLI4227.1).
- Saha, S., and Coauthors, 2010: The NCEP Climate Forecast System Reanalysis. *Bull. Amer. Meteor. Soc.*, **91**, 1015–1057, doi:[10.1175/2010BAMS3001.1](https://doi.org/10.1175/2010BAMS3001.1).
- Schubert, S. D., R. Rood, and J. Pfandtner, 1993: An assimilated dataset for Earth science applications. *Bull. Amer. Meteor. Soc.*, **74**, 2331–2342, doi:[10.1175/1520-0477\(1993\)074<2331:AADFES>2.0.CO;2](https://doi.org/10.1175/1520-0477(1993)074<2331:AADFES>2.0.CO;2).
- Schultz, M. G., and Coauthors, 2008: Global wildland fire emissions from 1960 to 2000. *Global Biogeochem. Cycles*, **22**, GB2002, doi:[10.1029/2007GB003031](https://doi.org/10.1029/2007GB003031).
- Schwartz, M. J., and Coauthors, 2008: Validation of the Aura Microwave Limb Sounder temperature and geopotential height measurements. *J. Geophys. Res.*, **113**, D15S11, doi:[10.1029/2007JD008783](https://doi.org/10.1029/2007JD008783).
- Seidel, D. J., and Coauthors, 2016: Stratospheric temperature changes during the satellite era. *J. Geophys. Res.*, **121**, 664–681, doi:[10.1002/2015JD024039](https://doi.org/10.1002/2015JD024039).
- Simmons, A. J., P. Poli, D. P. Dee, P. Berrisford, H. Hersbach, S. Kobayashi, and C. Peubey, 2014: Estimating low-frequency variability and trends in atmospheric temperature using ERA-Interim. *Quart. J. Roy. Meteor. Soc.*, **140**, 329–353, doi:[10.1002/qj.2317](https://doi.org/10.1002/qj.2317).

- , P. Berrisford, D. P. Dee, H. Hersbach, S. Hirahara, and J.-N. Thpaut, 2016: A reassessment of temperature variations and trends from global reanalyses and monthly surface climatological datasets. *Quart. J. Roy. Meteor. Soc.*, **143**, 101–119, doi:[10.1002/qj.2949](https://doi.org/10.1002/qj.2949).
- Stieglitz, M., A. Ducharne, R. D. Koster, and M. J. Suárez, 2001: The impact of detailed snow physics on the simulation of snow cover and subsurface thermodynamics at continental scales. *J. Hydrometeor.*, **2**, 228–242, doi:[10.1175/1525-7541\(2001\)002<0228:TIODSP>2.0.CO;2](https://doi.org/10.1175/1525-7541(2001)002<0228:TIODSP>2.0.CO;2).
- Susskind, J., J. Rosenfield, and D. Reuter, 1983: An accurate radiative transfer model for use in the direct physical inversion of HIRS and MSU temperature sounding data. *J. Geophys. Res.*, **88**, 8550–8568, doi:[10.1029/JC088iC13p08550](https://doi.org/10.1029/JC088iC13p08550).
- Takacs, L. L., M. J. Suárez, and R. Todling, 2016: Maintaining atmospheric mass and water balance in reanalyses. *Quart. J. Roy. Meteor. Soc.*, **142**, 1565–1573, doi:[10.1002/qj.2763](https://doi.org/10.1002/qj.2763).
- Taylor, K. E., D. Williamson, and F. Zwiers, 2000: The sea surface temperature and sea-ice concentration boundary conditions for AMIP II simulations. PCMDI Tech. Rep. 60, 28 pp. [Available online at <http://www-pcmdi.llnl.gov/publications/pdf/60.pdf>.]
- Trenberth, K. E., and L. Smith, 2005: The mass of the atmosphere: A constraint on global analysis. *J. Climate*, **18**, 864–875, doi:[10.1175/JCLI-3299.1](https://doi.org/10.1175/JCLI-3299.1).
- Turner, J., and Coauthors, 2004: The SCAR READER project: Toward a high-quality database of mean Antarctic meteorological observations. *J. Climate*, **17**, 2890–2898, doi:[10.1175/1520-0442\(2004\)017<2890:TSRPTA>2.0.CO;2](https://doi.org/10.1175/1520-0442(2004)017<2890:TSRPTA>2.0.CO;2).
- van der Werf, G. R., J. Y. Randerson, L. Giglio, G. J. Collatz, P. S. Kasibhatla, and A. F. Arellano Jr., 2006: Interannual variability in global biomass burning emissions from 1997 to 2004. *Atmos. Chem. Phys.*, **6**, 3423–3441, doi:[10.5194/acp-6-3423-2006](https://doi.org/10.5194/acp-6-3423-2006).
- Wargan, K., and L. Coy, 2016: Strengthening of the tropopause inversion layer during the 2009 sudden stratospheric warming: A MERRA-2 study. *J. Atmos. Sci.*, **73**, 1871–1887, doi:[10.1175/JAS-D-15-0333.1](https://doi.org/10.1175/JAS-D-15-0333.1).
- , S. Pawson, M. A. Olsen, J. C. Witte, A. R. Douglass, J. R. Ziemke, S. E. Strahan, and J. E. Nielsen, 2015: The global structure of upper troposphere–lower stratosphere ozone in GEOS-5: A multiyear assimilation of EOS Aura data. *J. Geophys. Res.*, **120**, 2013–2036, doi:[10.1002/2014JD022493](https://doi.org/10.1002/2014JD022493).
- , G. Labow, S. Frith, S. Pawson, and G. Partyka, 2017: Evaluation of the ozone fields in NASA's MERRA-2 reanalysis. *J. Climate*, **30**, 2961–2988, doi:[10.1175/JCLI-D-16-0699.1](https://doi.org/10.1175/JCLI-D-16-0699.1).
- WMO, 2014: Scientific assessment of ozone depletion: 2014. Global Ozone Research and Monitoring Project Rep. 55, 416 pp. [Available online at <https://www.esrl.noaa.gov/csd/assessments/ozone/2014/chapters/2014OzoneAssessment.pdf>.]
- Wu, W.-S., R. J. Purser, and D. F. Parrish, 2002: Three-dimensional variational analysis with spatially inhomogeneous covariances. *Mon. Wea. Rev.*, **130**, 2905–2916, doi:[10.1175/1520-0493\(2002\)130<2905:TDVAWS>2.0.CO;2](https://doi.org/10.1175/1520-0493(2002)130<2905:TDVAWS>2.0.CO;2).
- Xie, P., A. Yatagai, M. Chen, T. Hayasaka, Y. Fukushima, C. Liu, and S. Yang, 2007: A gauge-based analysis of daily precipitation over East Asia. *J. Hydrometeor.*, **8**, 607–626, doi:[10.1175/JHM583.1](https://doi.org/10.1175/JHM583.1).
- Yu, H., and Coauthors, 2006: A review of measurement-based assessments of the aerosol direct radiative effect and forcing. *Atmos. Chem. Phys.*, **6**, 613–666, doi:[10.5194/acp-6-613-2006](https://doi.org/10.5194/acp-6-613-2006).